A candidate relativistic tidal disruption event at 340 Mpc

Jean J. Somalwar [ID],[1] Vikram Ravi [ID],[1] Dillon Z. Dong [ID],[1] Yuyang Chen,[2,3] Shari Breen,[4] Poonam Chandra [ID],[5] Tracy Clarke [ID],[6] Kishalay De,[7] B. M. Gaensler [ID],[3,2] Gregg Hallinan [ID],[1] Sibasish Laha [ID],[8,9,10] Casey Law [ID],[1] Steven T. Myers,[11] Tyler Parsotan,[8,9,10] Wendy Peters [ID],[6] and Emil Polisensky[6]

[1]*Cahill Center for Astronomy and Astrophysics, MC 249-17 California Institute of Technology, Pasadena CA 91125, USA.*
[2]*David A. Dunlap Department of Astronomy and Astrophysics, University of Toronto, 50 St. George Street, Toronto M5S 3H4, Canada*
[3]*Dunlap Institute for Astronomy and Astrophysics, University of Toronto, 50 St. George Street, Toronto M5S 3H4, Canada*
[4]*SKA Observatory, Jodrell Bank, Lower Withington, Macclesfield, SK11 9FT, UK*
[5]*National Radio Astronomy Observatory, 520 Edgemont Road, Charlottesville VA 22903, USA*
[6]*Naval Research Laboratory, 4555 Overlook Ave SW, Washington, DC 20375, USA.*
[7]*MIT-Kavli Institute for Astrophysics and Space Research, 77 Massachusetts Ave., Cambridge, MA 02139, USA*
[8]*Center for Space Science and Technology, University of Maryland Baltimore County, 1000 Hilltop Circle, Baltimore, MD 21250, USA.*
[9]*Astrophysics Science Division, NASA Goddard Space Flight Center, Greenbelt, MD 20771, USA.*
[10]*Center for Research and Exploration in Space Science and Technology, NASA/GSFC, Greenbelt, Maryland 20771, USA*
[11]*National Radio Astronomy Observatory, P.O. Box O, Socorro, NM 87801, USA*

ABSTRACT

We present observations of an extreme radio flare, VT J024345.70-284040.08, hereafter VT J0243, from the nucleus of a galaxy with evidence for historic Seyfert activity at redshift $z = 0.074$. Between NRAO VLA Sky Survey observations in 1993 to VLA Sky Survey observations in 2018, VT J0243 rose from a $\sim$GHz radio luminosity of $\nu L_\nu \lesssim 10^{38}$ erg s^{-1} to $\nu L_\nu \sim 10^{40}$ erg s^{-1}, and still continues to brighten. The radio spectral energy distribution (SED) evolution is consistent with a nascent jet that has slowed over $\sim$3000 days with an average $0.1 < \langle\beta\rangle < 0.6$. The jet is energetic ($\sim 10^{51-52}$ erg), and had a radius $\sim$0.7 pc in Dec. 2021. X-ray observations suggest a persistent or evolving corona, possibly associated with an accretion disk, and IR and optical observations constrain any high-energy counterpart to be sub-Eddington. VT J0243 may be an example of a young, off-axis radio jet from a slowly evolving tidal disruption event. Other more mysterious triggers for the accretion enhancement and jet launching are possible. In either case, VT J0243 is a unique example of a nascent jet, highlighting the unknown connection between supermassive black holes, the properties of their accretion flows, and jet launching.

1. INTRODUCTION

In galactic nuclei, accretion-associated phenomena produce extreme radio variability on timescales of months−years and with flare luminosities covering the full range up to $\gtrsim 10^{32}$ erg s^{-1} Hz^{-1}. These flares are often associated with tidal disruption events (TDEs; Alexander et al. 2020), young radio jets from active galactic nuclei (AGN; Nyland et al. 2020; Mooley et al. 2016; Kunert-Bajraszewska et al. 2020; Wołowska et al. 2021), or outflows launched from accretion disks (e.g. Koay et al. 2016).

The physical mechanisms causing many of these radio flares in galactic nuclei have yet to be understood. For stellar mass black holes, it is well established that there is a strong connection between accretion and the launching of radio-emitting outflows and jets (see Fender 2010, for a review). Jet and outflow launching from supermassive black holes (SMBHs) is an unsolved problem, whether we consider those black holes associated with AGN that have been accreting for long timescales or the newly active black holes resulting from stellar dis-

ruptions. The conditions under which radio jets launch, the mechanisms through which they emit across the electromagnetic spectrum, and their duty cycle remain open questions (e.g. Blandford et al. 2019).

Our understanding of accretion-associated radio transients is evolving significantly with the advent of high-resolution, wide-field radio surveys, such as the Very Large Array Sky Survey (VLASS; Lacy et al. 2020). In this paper, we present an extraordinarily luminous radio transient discovered with VLASS, VT J024345.70-284040.08, hereafter VT J0243. VT J0243 is located in the nucleus of a nearby galaxy, 2dFGRS TGS314Z138 ($z = 0.0742$, Section 4.1). We identified VT J0243 as a radio transient between the NRAO VLA Sky Survey (NVSS; Condon et al. 1998) and VLASS. VT J0243 has risen to $\sim 10^{40}$ erg s^{-1} over $\sim$5 years, and continues to brighten. As we will show, VT J0243 is likely a nascent radio jet, yet no other event observed to date has shown its multiwavelength signatures, including a radio luminosity that continues to rise more than 1000 days after the jet turned on. In Section 2, we describe our se-

lection criteria that led to the discovery of VT J0243. In Section 3, we describe our multiwavelength archival searches and follow-up observations. In Section 4, we present our analysis of the observations, and in Section 5, we discuss the interpretation of VT J0243.

We adopt the Planck Collaboration et al. (2020) cosmology with $H_0 = 67.7$ km s^{-1} Mpc^{-1}.

2. TARGET SELECTION

VT J0243 was detected as part of our transient search using the 1.4 GHz NRAO VLA Sky Survey in the 1990s (Condon et al. 1998) and the 3 GHz VLA Sky Survey (Lacy et al. 2020), observing from 2017 to today. These surveys provide a unique opportunity to identify slowly evolving radio transients. NVSS has an rms noise 0.45 mJy/beam and a resolution of 45″ FWHM, and VLASS has an rms noise 0.14 mJy/beam and a resolution 1″.5 FWHM. Dong et al., in prep., generated a transient catalog by identifying sources that were detected by pyBDSF at a $> 7\sigma$ level in VLASS but were not detected ($< 3\sigma$) in NVSS. We refer the reader to that work and Appendix A of Somalwar et al. (2021) for a detailed description of the pipeline used.

VT J0243 was also selected as an evolving source in an independent search (Chen et al., in prep.) that identified young radio transients through VLASS and the VLITE Commensal Sky Survey (VCSS; Peters et al. 2021). VCSS is a survey conducted simultaneously with VLASS by VLITE, a commensal instrument on the VLA (Clarke et al. 2016; Polisensky et al. 2016). VCSS covers the same regions of the sky as VLASS and observes at $\nu \sim 340$ MHz with an angular resolution of $\theta \sim 20″$ and a median image rms of 3 mJy/beam. Additionally, VT J0243 was identified to be young because of its inverted spectrum between 340 MHz $-$ 3 GHz, suggesting optically thick emission at low frequencies.

Because of the extreme radio luminosity of this source given its history of inactivity and its coincidence with the nucleus of a low-mass galaxy, we initiated an extensive, multi-wavelength follow-up campaign.

3. OBSERVATIONS AND DATA REDUCTION

In this section, we describe our multi-wavelength follow-up of and archival searches for VT J0243 and its host, 2dFGRS TGS314Z138.

3.1. *Radio observations*

The available archival radio observations and our radio follow-up are summarized in Table 1. After a non-detection by NVSS on MJD 49520, VT J0243 was first detected on MJD 58166 in the first epoch of the VLASS with a luminosity $\nu L_\nu(3 \text{ GHz}) \sim 10^{40}$ erg s^{-1}. NVSS and VLASS are described at the beginning of Section 2. At the same time as the VLASS first epoch observations, VCSS detected the source (see Section 2 for details of VCSS). The source was then detected by the Autralian SKA Pathfinder (ASKAP) telescope as part of the Rapid ASKAP Continuum Survey (RACS) at 0.9 GHz McConnell et al. (2020). RACS is observing the whole sky visible to ASKAP in the 700$-$1800 MHz band with 15″resolution and a sensitivity of $\sim$0.25 mJy/beam. The final surveys to detect VT J0243 were the second epochs of VLASS and VCSS. Follow-up observations for this source were obtained using the Australia Telescope Compact Array (ATCA), the upgraded Giant Metrewave Radio Telescope (uGMRT), and the Very Long Baseline Array (VLBA).

Two epochs of ATCA observations were obtained on MJDs 59392 and 59439 with the six 22 m dishes arranged in the extended 6B configuration, providing baselines spanning 214–5969 m.[1]. The Compact Array Broadband Backend (CABB; Wilson et al. 2011) was used in the CFB-1M mode to simultaneously record full-polarization visibilities in two 2048 MHz bands each split into 2048 1 MHz channels. In the first epoch, by cycling between three different non-standard frequency setups data were obtained in 2048 MHz bands centered on 2.1 GHz, 5.25 GHz, 7 GHz, 8.75 GHz, and 10.25 GHz. Observations in the first epoch totaled two hours. Scans of PKS 1934$-$638 in each frequency setup were used to set the flux-density scale, and calibrate the complex time-independent bandpasses. Regular observations of the unresolved source PKS 0237$-$233 were used to calibrate the time-variable complex gains. In the second epoch, data were obtained at 5.25 GHz, 8.75 GHz, 18 GHz, 24 GHz, 34 GHz, 40 GHz in 2048 MHz bands to further constrain time evolution and spectral shape at high frequencies. For the cm bands, scans of PKS 1934-638 and PKS 0237-233 were again used to calibrate the bandpass, flux density scale, and time-variable gains. For the mm bands, scans of PKS 1921-293 were used instead of PKS 1934-638 for the bandpass and flux calibration.

The data were reduced, edited, calibrated and imaged using standard techniques implemented in the MIRIAD package (Sault et al. 1995). Multi-frequency synthesis images were made in multiple sub-bands, centered on frequencies listed in Table 1. VT J0243 was detected in all images; single rounds of phase-only self calibration were applied in each band to improve image quality. Flux densities and their uncertainties were estimated using the MIRIAD task imfit.

The event VT J0243 was observed with the upgraded Giant Metrewave Radio Telescope (uGMRT) under Director's Discretionary Time (DDT) proposal DDT C203 on 2021 Aug 27, 28 and 29 in bands 3 (250—500 MHz), 5 (1000– 1450 MHz) and 4 (550—900 MHz), respectively, of the uGMRT. The observations were two hours in duration including overheads using a bandwidth of 400 MHz in bands 4 and 5, whereas the duration was

---

[1] https://www.narrabri.atnf.csiro.au/observing/users_guide/html/chunked/aph.html

Table 1. Radio Observations

Instrument/Survey	Date	MJD	Frequency [GHz]	Flux Density [mJy]
NVSS[1]	Sept. 20 1993	49250	1.4	$< 1.3\ (3\sigma)$
TGSS[2]	Dec. 27 2010	55557	0.15	$< 15\ (3\sigma)$
VCSS[3] Epoch 1	Feb. 17, 2018	58166	0.340	23 ± 7
VLASS[4] Epoch 1	Feb. 17, 2018	58166	2.157	39.14 ± 0.31
VLASS Epoch 1	Feb. 17, 2018	58166	2.578	40.21 ± 0.26
VLASS Epoch 1	Feb. 17, 2018	58166	3.048	41.54 ± 0.30
VLASS Epoch 1	Feb. 17, 2018	58166	3.865	41.39 ± 0.34
RACS[5]	Apr. 28, 2019	58601	0.8875	45.81 ± 0.64
VCSS Epoch 2	Nov. 1, 2020	59154	0.340	22 ± 7
VLASS Epoch 2	Nov. 1, 2020	59154	2.157	54.33 ± 0.48
VLASS Epoch 2	Nov. 1, 2020	59154	2.579	53.85 ± 0.34
VLASS Epoch 2	Nov. 1, 2020	59154	3.048	52.84 ± 0.29
VLASS Epoch 2	Nov. 1, 2020	59154	3.685	52.29 ± 0.34
ATCA Epoch 1 (PC: CX486)	Jun. 27, 2021	59392	1.877	68.82 ± 11.51
ATCA Epoch 1 (PC: CX486)	Jun. 27, 2021	59392	2.636	71.26 ± 12.69
ATCA Epoch 1 (PC: CX486)	Jun. 27, 2021	59392	4.79	59.23 ± 6.59
ATCA Epoch 1 (PC: CX486)	Jun. 27, 2021	59392	5.779	55.92 ± 6.24
ATCA Epoch 1 (PC: CX486)	Jun. 27, 2021	59392	6.732	52.48 ± 5.34
ATCA Epoch 1 (PC: CX486)	Jun. 27, 2021	59392	7.734	49.27 ± 5.22
ATCA Epoch 1 (PC: CX486)	Jun. 27, 2021	59392	8.706	46.49 ± 4.9
ATCA Epoch 1 (PC: CX486)	Jun. 27, 2021	59392	9.677	45.08 ± 4.98
ATCA Epoch 1 (PC: CX486)	Jun. 27, 2021	59392	10.68	43.61 ± 5.56
ATCA Epoch 2 (PC: CX486)	Aug. 13, 2021	59439	5.25	57.47 ± 0.7
ATCA Epoch 2 (PC: CX486)	Aug. 13, 2021	59439	8.75	48.74 ± 0.52
ATCA Epoch 2 (PC: CX486)	Aug. 13, 2021	59439	18.0	32.0 ± 0.66
ATCA Epoch 2 (PC: CX486)	Aug. 13, 2021	59439	34.0	21.4 ± 0.71
ATCA Epoch 2 (PC: CX486)	Aug. 13, 2021	59439	40.0	19.82 ± 0.69
GMRT (PID: ddtC203)	Aug. 27, 2021	59454	0.402	32.39 ± 0.24
GMRT (PID: ddtC203)	Aug. 29, 2021	59454	0.648	52.44 ± 0.26
GMRT (PID: ddtC203)	Aug. 28, 2021	59454	1.264	60.88 ± 0.41

NOTE—Archival and follow-up radio observations of VT J0243. References: [1](Condon et al. 1998), [2](Intema et al. 2017), [3](Peters et al. 2021), [4](Lacy et al. 2020), [5](McConnell et al. 2020).

three hours in band 3. The VLA calibrator 3C 147 was used as a flux and a bandpass calibrator and J0240-231 was used as a phase calibrator. We use the Common Astronomy Software Applications (CASA; McMullin et al. 2007) for data analysis. The data were analyzed in three major steps, i.e flagging, calibration and imaging using the procedure laid out in Maity & Chandra (2021). A total of 6 rounds of phase self-calibrations and 2 rounds of amplitude & phase self-calibration were performed. A source was clearly detected at the VLASS position. The

source flux densities at bands 5, 4 and 3 are mentioned in Table 1.

VLBA observations of VT J0243 were conducted on MJD 59569, with 512 MHz of bandwidth centered on 8.368 GHz, and the data were processed using the DiFX correlator (Deller et al. 2011). Data were recorded at a rate of 4.096 Gbps at all sites besides North Liberty in four 128 MHz sub-bands, using the Digital Down-converter (DDC) mode of the Roach Digital Backends. Given the high expected flux density of the source, we planned to self-calibrate the observations. The 45 min

observation included two 2 min scans of the fringe finder J0555+3948, and two 1 min scans of the check source J0236-2953, and a total of 31.5 min on VT J0243. Calibration and imaging of the observations was carried out using CASA, following procedures outlined in VLBA Memo 38.[2] Following data editing, we performed a global fringe-fit, which was successful for seven antennas (data from Pie Town and St. Croix were substantially lower in sensitivity). We then performed two rounds of phase-only self-calibration on VT J0243, and one round of amplitude+phase self-calibration. This yielded phase variations under ± 5 deg. An image of and inspection of visibility amplitudes on VT J0243 revealed a partially resolved source. We fit the data with an elliptical Gaussian model using the CASA task uvmodelfit, and found a flux density of 37 mJy (with $\sim 10\%$ uncertainty), a major axis of 1.1 ± 0.1 mas, and a minor axis of 0.5 ± 0.1 mas, at a position angle of -23 deg.

3.2. Optical photometry

From the radio observations of VT J0243, we can naively constrain the radio-turn-on time range to $1990-2018$. The Catalina Realtime Transient Survey (CRTS; Drake et al. 2009) observed the location of VT J0243 between ~ 2005 and 2013 (MJD $53554-56302$), the Pan-STARRS 3π survey (Chambers et al. 2016) over $\sim 2010-2013$ (MJD $55433-56970$), and the Asteroid Terrestrial-impact Last Alert System (ATLAS; Tonry et al. 2018) between $\sim 2015-2021$ (MJD $57303-59097$). We retrieve the CRTS photometry for this source from the default photcat catalog (Drake et al. 2009). This photometry is performed on absolute (i.e., not difference) images using SExtractor to measure aperture magnitudes. Also note that CRTS does not use a filter, so the absolute calibration of the photometry is uncertain. We retrieved archival optical images of the source from the PanSTARRS1 survey (Chambers et al. 2016). The reduced images were processed through a custom image subtraction pipeline (described in De et al. 2020) to remove the host galaxy light using the first epoch of PS1 observations as a template. Point-spread function photometry was performed on the resulting difference images to derive the optical light curve shown in Figure 1. We retrieve ATLAS photometry at the position of 2dFGRS TGS314Z138 from their forced photometry server[3] using default settings. Finally, we generated a mid-infrared lightcurve for VT J0243 by performing PSF photometry on single-epoch difference images from the UNWISE reprocessing of observations from the WISE and NEOWISE surveys (Lang 2014; Meisner et al. 2017; Wright et al. 2010; Mainzer et al. 2011). The resulting lightcurves are summarized in Figure 1.

3.3. Optical spectroscopy

An optical spectrum of VT J0243 was obtained before 2002 (MJD < 52375) as part of the 2dF Galaxy Redshift Survey (2dFGRS; Cole et al. 2005). The spectrum was taken using a $2''0$ arcsec fiber with the 2dF instrument on the Anglo-Australian Telescope telescope. The wavelength range was $3627-8037$ Å (observed frame) and the resolution $R = 648$. We retrieved the non-flux calibrated spectrum from the NASA/IPAC Extragalactic Database (NED). We observed VT J0243 on the night of Oct. 6 2021 (MJD 59493) using the Low Resolution Image Spectrometer (LRIS; Oke et al. 1995) on the Keck I telescope. We used the $1''0$ slit centered on the galactic nucleus using a parallactic angle $(-0.035°)$. We used the 400/3400 grism, the 400/8500 grating with central wavelength 7830, and the 560 dichroic. We observed this source for 20 min. The resulting wavelength range was $\sim 1300-10000$ Å and the resolution $R\sim 700$. Comparing these spectra, there are no obvious transient features (Figure 1). Weak AGN-like emission lines are visible, but no broad emission lines are detected. The spectra are all fully consistent with being host-dominated.

3.4. X-ray/UV observations

VT J0243 was observed in the X-ray band as part of the ROSAT survey on Jan. 6, 1990 (MJD 47897). There is no detection reported in the Second ROSAT All-Sky Survey Point Source Catalog (Voges 1993; Boller et al. 2016). We retrieved the ROSAT image at the location of VT J02438 from the HEASARC archive[4], and used ximage to find a 3σ upper limit of the $0.3-10$ keV, unabsorbed soft X-ray flux, $f_X \lesssim 2 \times 10^{-13}$ erg cm^{-2} s^{-1}, assuming a power law spectrum with $\Gamma = 3$ and the Milky Way $N_{H,MW} = 1.51 \times 10^{20}$ cm^{-2} (HI4PI Collaboration et al. 2016). VT J0243 was subsequently observed by the XMM-Newton Slew Survey on Jul. 30, 2008 (MJD 54677), Dec. 30, 2009 (MJD 55195), Jul. 12, 2012 (MJD 56120), Jan. 26, 2021 (MJD 59240), and Jun. 26, 2021 (MJD 59391). No detection was reported on any of these dates, so we adopt an upper limit corresponding to the flux limit reported by the survey $f(0.2-12 \text{ keV}) = 1.3 \times 10^{-12}$ erg s^{-1} cm^{-2} $(L \sim 1.67 \times 10^{43}$ erg s$^{-1})$. Finally, VT J0243 was observed by the Monitor of All-sky X-ray Image (MAXI; Matsuoka et al. 2009). We retrieved $2-30$ keV photometry for this transient using the on-demand photometry survey provided by the MAXI collaboration[5] for the MJD range $55058.0-58000.0$. No significant detection was reported, and the typical upper limit was $f_X(0.3-10 \text{ keV}) \lesssim 7.7 \times 10^{-11}$ erg s^{-1} cm^{-2}. There was also no significant detection by the Swift Burst Area Telescope (BAT) in the transient monitor light

[2] https://library.nrao.edu/public/memos/vlba/sci/VLBAS_38.pdf
[3] https://fallingstar-data.com/forcedphot/
[4] https://heasarc.gsfc.nasa.gov/docs/archive.html
[5] http://maxi.riken.jp/mxondem/

curve produced for this source during the MJD range 55798−56961 (Krimm et al. 2006).

We observed VT J0243 using the X-ray Telescope (XRT) on The Neil Gehrels Swift Observatory (Swift XRT; Burrows et al. 2005) on MJD 59379 and 59484 for 3 and 5 ks exposures, respectively. A source was detected in both exposures, with $0.3 - 10$ keV fluxes of $0.67 \pm 0.35 \times 10^{-13}$ erg cm^{-2} s^{-1} and 1.28 ± 0.37 cm^{-2} s^{-1}, respectively, assuming power-law spectra with $\Gamma = 3$. We then obtained a soft X-ray spectrum for VT J0243 on MJD 59391 using the *XMM*-Newton observatory EPIC camera using the thin filters in full frame mode with a 30 ks exposure time. We used the standard analysis pipeline to process the data and extract an X-ray spectrum.

Swift/UVOT observed VT J0243 simultaneously with the Swift/XRT observations in the UVW1 band. We reduced the observations using the standard HEA-SOFT pipeline and measured the source magnitude using the `uvotsource` tool with a 5″source region and a 15″background region offset from the source. We found a UVW1 AB magnitude 20.38 ± 0.06(stat) ± 0.03(sys). This is consistent within 2σ with the quiescent-level predictions from our SED fit (see Section 4.1), so there is no detectable transient emission and we do not consider these observations further.

4. ANALYSIS

In this section, we present our analyses of the archival and follow-up observations of VT J0243. We begin in Section 4.1 with a brief discussion of the host properties. In Section 4.2, we constrain the physical properties of the radio-emitting outflow or jet using the radio observations. In Section 4.3 we constrain the origins of the X-ray emission, and in Section 4.4, we discuss the optical and infrared photometry at the location of VT J0243.

4.1. *Host Galaxy*

VT J0243 is offset by $0.2''$(1σ uncertainty $\sim 0''.15$) from the Pan-STARRS centroid of the galaxy 2dFGRS TGS314Z138. 2dFGRS TGS314Z138 is an SA galaxy. We summarize relevant properties of this host in Table 2, including its redshift and location. In this section, we will constrain the star formation rate, stellar and black hole mass, and BPT classification of this galaxy. We will use these properties to constrain the origin of the emission associated with VT J0243 and the trigger of VT J0243 later in this work.

To measure the stellar mass and star formation history of the galaxy, we performed an SED fit using the `Prospector` code (Johnson et al. 2021; Conroy & Gunn 2010; Conroy et al. 2009) and the WISE, GALEX, and Pan STARRS galaxy photometry following a similar procedure to Somalwar et al. (2021) and references therein. We assume a tau-model star formation history (SFR$\propto e^{-t/\tau}$), a Chabrier (2003) IMF, and extinction

Table 2. Host Galaxy, 2dFGRS TGS314Z138

Parameter	Value
R.A. (J2000)	02:43:45.70
Dec. (J2000)	-28:40:40.08
Redshift z	0.0742
d_L	347.0 Mpc
$\log M_*/M_\odot$	$10.28^{+0.06}_{-0.14}$
$t_{\rm age}$ [Gyr]	$1.6^{+5.4}_{-0.4}$
τ_2	$0.69^{+0.034}_{-0.028}$
[M/H]	$-1.23^{+0.14}_{-0.16}$
$t_{\rm burst}$	$0.3^{+5.4}_{-0.2}$
$f_{\rm burst}$	$0.78^{+0.11} + -0.34$
$\log M_{\rm BH}/M_\odot$ (from $M_{\rm BH} - M_*$)	6.94 ± 0.82

NOTE—R.A. and Dec. are from the Legacy imaging survey (York et al. 2000). Redshift is as measured in our work. The parameters below the line are derived from an SED fit using `fsps` and `prospector` (Johnson et al. 2021; Conroy et al. 2009; Conroy & Gunn 2010). dust2 is the SMBH mass is measured using the Greene et al. (2020) $M_{\rm BH} - M_*$ relation.

following Calzetti et al. (2000). We use `emcee` (Foreman-Mackey et al. 2013) to fit the SED, with 100 walkers, 500 burn-in steps, and 50000 steps. The results showed that τ was very small, with a posterior distribution rising towards $\tau < 0.1$ Gyr and flattening for lower values. `prospector` does not support such low values of τ, so we reran the fit including a burst component (i.e., a delta function of star formation) and fixing $\tau = 0.1$ Gyr. We found the fraction of the stellar mass formed in the burst was poorly constrained but peaked towards 1. The age of the burst is also poorly constrained. We report the maximum-a-posteriori estimate and 1σ highest posterior density interval for each fit parameter in Table 2

First, we consider the star formation rate of this galaxy. The star formation rate is critical for constraining the source of the observed X-ray emission (Section 4.3). Our SED fitting results were consistent with a large fraction of the stellar mass forming in a star formation burst near the lookback time at $z = 0.0742$. Hence, the star formation rate could be very high for this source ($\gtrsim 1 M_\odot$ yr^{-1}). However, our constraints are sufficiently loose that the SFR may be $\ll 1 M_\odot$ yr^{-1}. For galaxies with star formation that has remained constant for $\sim$6 Myrs, the Hα−SFR relationship can be used to set an upper limit on the SFR as SFR$= 5.5 \times 10^{-42} L_{\rm H\alpha} \sim 0.21 M_\odot$ yr^{-1}, with $\sim$15% uncertainty Calzetti (2013). We measured $L_{\rm H\alpha} = (3.73 \pm 0.05) \times 10^{40}$ erg s^{-1}, before any host extinction corrections. If we use the Hα/Hβ ratio to measure the host extinction, we find
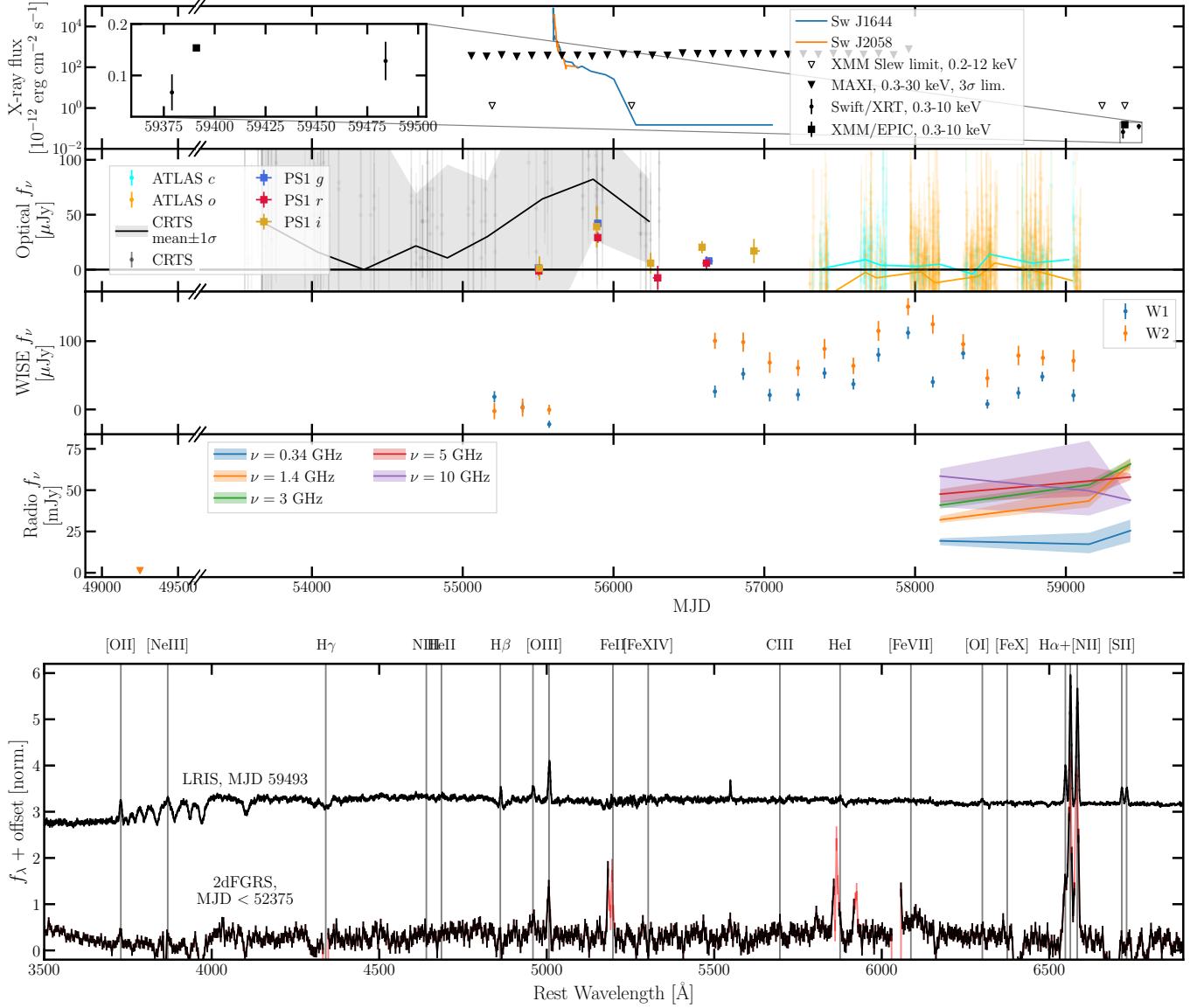
Figure 1. (*top*) From top to bottom, X-ray, optical, mid-infrared, and radio lightcurves for VT J0243. In the topmost panel, the black triangles represent three sigma upper limits from the MAXI and XMM slew surveys. The squares and circles show recent detections by Swift/XRT and XMM/EPIC, and the inset axis magnifies this data. The colored lines show the X-ray lightcurves for two of the three X-ray detected jetted TDEs, Sw J1644+57 (Levan et al. 2016) and Sw J2058+05 (Pasham et al. 2015). We do not show the X-ray lightcurve for the final X-ray detected jetted TDE, Sw J1112-8283 (Brown et al. 2017), as it largely overlaps with the Sw J1644+57 lightcurve but is poorly sampled in comparison. Regardless of the binning of the MAXI observations, an X-ray flare of the same luminosity as those detected for previous jetted TDEs would have been detected in the first ∼100 days. An optical flare is detected in PanSTARRS around MJD 56000. The MIR emission is measured using forced photometry on NEOWISE images, and is variable. The MIR color appears to have reddened after the first three epochs. The radio lightcurves are extrapolated from the model fits described in Section 4.2, and the non-detection on the far left of the plot corresponds to the 1990 NVSS observation. (*bottom*) LRIS (*top*) and 2dFGRS (*bottom*) optical spectra, normalized. No significant transient features are detected. No broad emission lines are significantly detected. The emission line ratios are consistent with weak Seyfert emission on a BPT diagram.

$$A_{\mathrm{H}\alpha} = (3.33 \pm 0.80) \times 1.97 \log \left(\frac{\mathrm{H}\alpha/\mathrm{H}\beta}{2.86} \right) = 1.09 \pm 0.26$$

(Domínguez et al. 2013). Then, the extinction corrected Hα luminiosity is $L_{\mathrm{H}\alpha,0} = (10.2 \pm 2.5) \times 10^{40}$

erg s^{-1}. Plugging this luminosity into the Hα-SFR relationship, we find SFR$= 0.56 \pm 0.16$; in other words SFR$< 1\,M_\odot$ yr^{-1} at the 3σ level. We find a similar constraint using the [O II] luminosity and the SFR-[O II] relation from Kewley et al. (2006). These constraints are robust even if the line emission is not entirely produced by star formation (see the end of this section for a discussion of possible AGN activity in 2dFGRS TGS314Z138). However, the Hα constraint relies on the assumption that the star formation has been constant for at least 6 Myrs.

Next we use the stellar mass of 2dFGRS TGS314Z138 to constrain the black hole mass of the galaxy. The black hole mass is critical for constraining the origin of VT J0243, as different types of transients dominate at different masses (e.g., TDEs cannot occur for $M_{\rm BH} \gtrsim 10^8\,M_\odot$). The stellar mass of this galaxy is well-constrained at $\log M_* = 10.06^{+0.12}_{-0.08}$. Using the black hole-stellar mass relation from Greene et al. (2020), we find a black hole mass $\log M_{\rm BH}/M_\odot = 6.94 \pm 0.82$.

Finally, we discuss the optical spectral features, and use them to classify 2dFGRS TGS314Z138 as a possible Seyfert galaxy. Both the archival 2dFGRS and the LRIS spectra show narrow line emission associated with AGN, such as [O III] $\lambda\lambda 4959, 5007$, H$\beta$, H$\alpha$, [N II]$\lambda\lambda 6548, 6583$, and [S II]$\lambda\lambda 6716, 6731$. We fit the spectra and measure emission line strengths using the same procedures as Somalwar et al. (2021), and we refer the reader to that work for details. There has been no significant evolution in any of the line ratios, so we assume that the recent LRIS spectrum does not include any transient emission associated with VT J2043 and place both spectra on BPT diagrams (Baldwin et al. 1981; Kewley et al. 2006; Cid Fernandes et al. 2011), as shown in Figure 2. Both spectra are consistent with BPT-weak Seyferts. Likewise, none of the available WISE mid-infrared colors of 2dFGRS TGS314Z138 are consistent with a strong AGN (Assef et al. 2018). We thus identify this galaxy as a weak Type 2 Seyfert. As we will discuss in Section 4.3, this galaxy may be a *true* Type 2 Seyfert, meaning that the absence of broad lines may be due to the complete lack of a broad line region (BLR). From the ROSAT soft X-ray flux constraints, we can constrain the pre-flare AGN accretion rate. Since $L_X \lesssim 2.6 \times 10^{42}$ erg s$^{-1} \lesssim 10^{-3}L_{\rm edd.}$ and assuming a bolometric correction ~ 20 (Lusso et al. 2012), we find $f_{\rm edd.} \lesssim 2\%$.

4.2. *Radio analysis*

Typically, radio emission from galactic centers is dominated by synchrotron emission due to particles accelerated within a relativistic, collimated jet (Blandford et al. 2019) or shocks from the collision of a jet and/or non-relativistic, wide-angle outflow with the circumnuclear medium (CNM). This emission can be self-absorbed or free-free absorbed. Because we are observing a transient, the outflow or jet must be expanding. In this section, we combine a fit to our VLBA observations of this source with synchrotron modelling of the observed SED (Figure 3) to constrain the physical parameters of the source.

4.2.1. *Synchrotron analysis methods*

We constrain the physical properties of the source by assuming equipartition between the energy in electrons and the energy in the magnetic field. We also adopt the standard assumption that the relativistic electron distribution is a power-law in Lorentz factor (LF) above a minimum LF γ_m: $N(\gamma)d\gamma = N_0\gamma^{-p}d\gamma$, $\gamma > \gamma_m$. In this case, the SED is well-modelled by a broken power law (Chevalier 1998; Granot & Sari 2002).

The slopes of the power law segments depend on the ordering of a number of characteristic LFs. The three relevant LFs for this work are (1) the LF of the lowest energy electrons γ_m, (2) the electron energy at which the optical depth to synchrotron self-absorption is one, $\gamma_{\rm sa}$, and (3) the energy at which the electron cooling timescale is shorter than the age of the source, γ_c. Each of these corresponds to a characteristic synchrotron frequency $\nu_{\rm x} = \gamma_{\rm x}^2 eB/(m_e c)$, ${\rm x} \in [m, {\rm sa}, c]$, where e is the electron charge, B is the magnetic field strength, and m_e is the electron mass. These characteristic frequencies correspond to the locations of the breaks in a multiply-broken power law model of the synchrotron emission.

Our radio SED at all epochs is best-modelled when $\nu_{\rm sa} < \nu_m < \nu_c$. No other orderings can reproduce the observed broad and flat peak. For $\nu_{\rm sa} < \nu_m < \nu_c$, the power-law slope in the optically thick regime ($\nu < \nu_{\rm sa}$) is 2, corresponding to the slope of a Rayleigh-Jeans law with constant brightness temperature. For $\nu_{\rm sa} < \nu < \nu_m$, the slope is 1/3, which is that of a single electron spectrum at frequencies smaller than the characteristic synchrotron frequency of that electron. For $\nu_m < \nu$, the power-law slope is $\alpha = -(p-1)/2$. Since each electron primarily emits at its characteristic synchrotron frequency $\nu \propto \gamma^2$ and the synchrotron power for a single electron $-\frac{dE}{dt} \propto \gamma^2$, we can approximate the flux density $S_\nu(\nu)d\nu = -\frac{dE}{dt}N(\gamma)d\gamma \propto \gamma^{2-p}d\gamma \propto \nu^{-(p-1)/2}d\nu$, leading to the slope $\alpha = -(p-1)/2$.

Following Barniol Duran et al. (2013), we can now derive expressions for the number of electrons in the outflow N_e, magnetic field B, and total energy E as a function of radius R, bulk Lorentz factor Γ, and radio SED properties. We assume a fraction ϵ_e of the total energy is stored in electrons, and a fraction ϵ_B is stored in the magnetic field. We nominally assume $\epsilon_e = \epsilon_B = 0.1$, although at the end of this section we will vary those values. We assume the outflow has an area $f_A \pi R^2/\Gamma^2$ and volume $f_V \pi R^3/\Gamma^4$. As we will discuss, VT J0243 has transitioned to a regime where $\Gamma \sim 1$, so the following
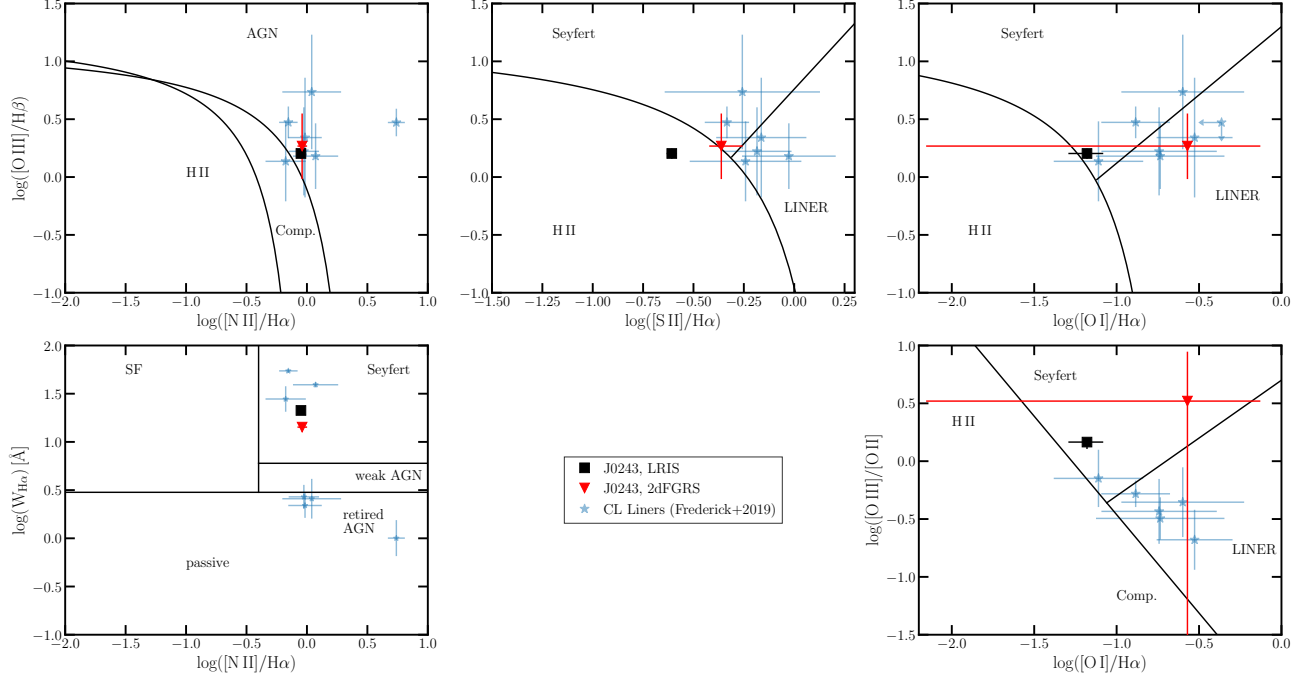
Figure 2. Five versions of the BPT diagram (Baldwin et al. 1981; Kewley et al. 2006; Cid Fernandes et al. 2011), following Figure 13 from Frederick et al. (2019). Line ratios measured from the LRIS (2dFGRS) observations of 2dFGRS TGS314Z138 are shown as black squares (red trangles). 2dFGRS TGS314Z138 is consistent with a Seyfert in most of the diagrams.

equations apply to the nonrelativistic limit.

$$N_e = \frac{9cF_p^3 d_L^6 \eta^{\frac{10}{3}} \Gamma^2}{2\sqrt{3}\pi^2 e^2 m_e^2 \nu_p^5 (1+z)^8 f_A^2 R^4} \approx 3.1 \times 10^{52} \frac{F_{p,-25}^3 \eta^{\frac{10}{3}} \Gamma^2}{\nu_{p,9}^5 R_{18}^4},$$
$$(1)$$

$$B = \frac{8\pi^3 m_e^3 c \nu_p^5 (1+z)^7 f_A^2 R^4}{9e F_p^2 d_L^4 \eta^{\frac{10}{3}} \Gamma^3} \approx 0.18\,\mathrm{G}\left(\frac{\nu_{p,9}^5 R_{18}^4}{F_{p,-25}^2 \eta^{\frac{10}{3}} \Gamma^3}\right),$$
$$(2)$$

$$E = \frac{1}{\epsilon_B} \frac{f_V R^3 B^2}{8\Gamma^2} \approx 5.3 \times 10^{51}\,\mathrm{erg}\left(\frac{1}{\epsilon_B} \frac{R_{18}^3 B_{-0.74}^2}{\Gamma^2}\right).$$
$$(3)$$

Here, d_L is the luminosity distance, F_p is the peak flux density, ν_p is the peak frequency, and z is redshift. The notation Y_x denotes quantity Y in units of 10^x cgs. The variable η is defined as the ratio between the minimum and self-absorption frequencies: $\eta = \nu_m/\nu_{sa}$ if $\nu_a < \nu_m$; else 1. Only the final equation for total energy E assumes equipartition. In the final equalities, we have adopted the luminosity and redshift of VT J0243. We also assume, both in these equalities and henceforth, that $f_A = 1$ and $f_V = 4/3$, appropriate for a spherical, nonrelativistic outflow. For a jet, the appropriate values are $f_A = f_V = (\theta_j \Gamma)^2$, where θ_j is the jet half-opening angle. For the jetted TDE Sw J1644, assuming $\theta_j \sim 0.1$, we have $f_A, f_V \gtrsim 0.1$ (Eftekhari et al. 2018).

We will also require the electron density of the material into which the outflow is expanding. We denote this density n_e. Note that $n_e \neq N_e/(4\pi R^3)$, since N_e is the electron number *in* the outflow, whereas n_e is the density of the material *outside* the outflow. We derive this density following Ho et al. (2019), who require conservation of momentum across the shock front and find

$$n_e = \frac{B^2}{6\pi\epsilon_B \beta^2 c^2 m_p} \approx 1.1\,\mathrm{cm}^{-3}\left(\frac{\nu_{p,9}^{10} R_{18}^8}{F_{p,-25}^4 \eta^{\frac{20}{3}} \Gamma^6 \beta^2 \epsilon_B}\right).$$

Here, $\beta = v/c$, where v is the outflow velocity. This equation assumes expansion of a thermal gas ($\gamma = 5/3$) into fully ionized hydrogen. The generalization to a relativistic gas would modify this equation by a factor of order unity, which we neglect as it is significantly smaller than our measurement errors.

To apply these equations, we require a measurement of η. The self-absorption frequency of this system is likely at or below the low frequency end of our observations, so we cannot tightly constrain η by fitting for ν_{sa} and ν_m. Instead, we use the outflow size measured using our VLBA observations. Under equipartition, the outflow
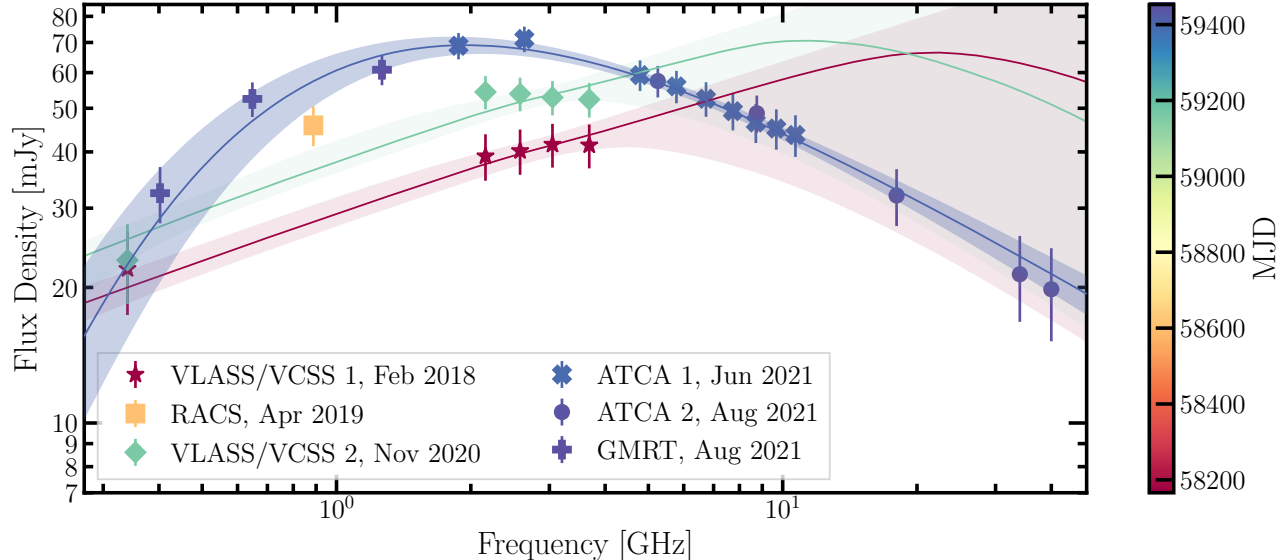
Figure 3. The evolution of VT J0243's radio SED. The circles with errorbars correspond to our observations, and are colored with the observation epoch. We fit a synchrotron model to the three main observation epochs (see Section 4.2 for details), and show the best-fit model and 1σ errors as lines and bands.

radius is related to η as

$$R = \left[\frac{3^7 c}{32\sqrt{3}\pi^9 m_e^8}\frac{p-1}{p-2}\frac{\epsilon_B}{\epsilon_e}\right]^{\frac{1}{17}}\frac{\Gamma^{\frac{11}{17}}F_p^{\frac{8}{17}}\eta^{\frac{35}{51}}d_L^{\frac{16}{17}}}{f_V^{\frac{1}{17}}(1+z)^{\frac{25}{17}}f_A^{\frac{7}{17}}\nu_p}$$

$$\approx 6.1\times10^{17}\,\mathrm{cm}\left[\left(\frac{p-1}{p-2}\frac{\epsilon_B}{\epsilon_e}\right)^{\frac{1}{17}}\frac{\Gamma^{\frac{11}{17}}F_{p,-25}^{\frac{8}{17}}\eta^{\frac{35}{51}}}{(1+z)^{\frac{25}{17}}\nu_{p,9}}\right].$$

4.2.2. *Synchrotron analysis results*

In this section, we present the physical parameters derived from our synchrotron analysis. First, however, we consider the fact that our observations can only be fit in the regime $\nu_{\mathrm{sa}} < \nu_m < \nu_c$. This is unusual − the Granot & Sari (2002) model for an adiabatically expanding outflow applied to this source suggests that we should observe $\nu_{\mathrm{sa}} > \nu_m$ given the > 1000 day age of the outflow. A very high ν_m at late times requires a source of energy which keeps the electron population at high γ. Thus, continual energy injection could explain our observation of $\nu_{\mathrm{sa}} < \nu_m$. Continual energy injection is also a possible explanation of the unusual, rising late-time radio light curve (Figure 1; also see Section 5)

To derive the physical parameters, we first constrain F_p and ν_p. We fit a doubly-broken power-law to the most recent observation epochs (GMRT+ATCA 1+ATCA 2) using the `dynesty` software (Speagle 2020). We fix the slopes to the expected values described above, and allow the position of each break and the electron spectral index p to float. We adopt broad, Heaviside priors on all parameters, except for p, which we require be in the physically-motivated range $[2, 5]$. We use the

resulting best-fit model to evaluate the peak flux density and frequency, along with their uncertainties. We find $F_p = 66.7 \pm 3.1$ mJy, $\nu_p = 2.28 \pm 0.28$ GHz, and $p = 2.40 \pm 0.17$. Note that the peak frequency is consistent within $< 2.5\sigma$ with the best-fit characteristic minimum frequency, $\nu_m = 2.78 \pm 0.35$ GHz. Next, we constrain the bulk lorentz factor, Γ. The outflow was launched before the first VLASS observation epoch on MJD 58166; hence, it is at least ~ 1400 days old. It was launched after the NVSS observation, so it is no more than ~ 10000 days old, Thus, we have $0.1 < \langle\beta\rangle \lesssim 0.6$ and average bulk Lorentz factor $1.005 < \Gamma \lesssim 1.3$.

Next, we calculate η using the outflow size and the equipartition radius equation. As described in Section 3, our VLBA observations imply an approximate radius $R = 0.71 \pm 0.02$ pc. Thus, we have $\eta = 5.17 \pm 1.13\,(\Gamma = 1.005), 4.05 \pm 0.89\,(\Gamma = 1.3)$. In both cases, the predicted ν_{sa} is consistent with constraints from our doubly-broken power-law fit. We reran the doubly-broken power-law fit while requiring η be consistent with the above values and found that p has not changed significantly from our previous measurement: $p = 2.20 \pm 0.12$.

Finally, we constrain the magnetic field, electron number density, and total energy. The results are tabulated in Table 3. The measured densities are consistent with results for other galaxies: at a similar distance (in units of the Schwarzschild radius), typical densities are $\gtrsim 10^{-1}$ cm^{-3} (see Fig. 2 of Alexander et al. 2020). The energies are consistent with jetted TDE observations (Eftekhari et al. 2018).

Table 3. Synchrotron Analysis Results

p	$\frac{R}{\mathrm{pc}}$	ϵ_e, ϵ_B	Γ	η	$\log \frac{B}{10^{-2}\mathrm{G}}$	$\log \frac{n_e}{\mathrm{cm}^{-3}}$	$\log \frac{E}{\mathrm{erg\,s}^{-1}}$
2.2 ± 0.12	0.71 ± 0.02	$0.1, 0.1$	1.005	5.2 ± 1.1	2.74 ± 0.82	1.32 ± 0.16	52.02 ± 0.16
			1.3	4.05 ± 0.89	3.0 ± 0.2	-0.11 ± 0.20	51.88 ± 0.20
		$0.1, 10^{-3}$	1.005	5.2 ± 1.1	0.70 ± 0.15	2.23 ± 0.14	52.81 ± 0.14
			1.3	4.05 ± 0.89	0.75 ± 0.23	0.69 ± 0.17	52.64 ± 0.17

Our assumption of $\epsilon_B = 0.1$ has been shown to be incorrect for the jetted TDE Sw J1644+57 (Eftekhari et al. 2018). If we adopt the preferred value for that event, $\epsilon_B = 10^{-3}$, our physical parameters are modified, and the results are listed in Table 3. The energy is now higher than measured for previous jetted TDEs (Eftekhari et al. 2018). A collimated geometries (i.e., smaller f_A and f_V) will tend to decrease the energy ($E \propto f_V^{3/7}$), increase the magnetic field ($B \propto f_V^{3/7}$), and increase n_e ($n_e \propto f_V^{6/7}$).

The evolution of VT J0243's radio SED is shown in Figure 3. The datapoints are colored by the observation MJD. We have overplotted a doubly-broken power law fit to the most recent epoch in purple. We overplot fits to the VLASS/VCSS observations. In these fits, p is forced to be consistent with the value measured from the most recent observations. The break frequencies and amplitude are allowed to float freely. These observations are not sufficiently well-sampled to provide strong constraints on any physical parameters, but are roughly consistent with expectations for an expanding outflow.

In summary, VT J0243 is associated with a luminous, energetic outflow. The outflow is currently non-relativistic, but given the high, and still rising, luminosity, we believe it likely that we are observing a relativistic jet, possibly off-axis, that has slowed. This hypothesis is supported by the observed non-spherical geometry from the VLBA (see the end of Section 3.1).

4.3. X-ray analysis

In this section, we discuss our X-ray observations. First, we present constraints on X-ray emission at the time that VT J0243 turned on. Then, we discuss the luminosity and spectrum from our more recent X-ray observations. Finally, we consider three possible origins for this late-time X-ray emission: star formation, an accretion disk, or something associated with the transient event.

Beginning on MJD $\sim$59375, we detected near-constant X-ray emission from the location of VT J0243 with a $0.3 - 10$ keV luminosity of $\log L_{0.3-10\,\mathrm{keV}}/(\mathrm{erg\,s}^{-1}) = 42.3 \pm 0.01$ (Figure 1), after correcting for Milky Way H I absorption ($N_{H,\mathrm{MW}} = 1.51 \times 10^{20}$ at the location of VT J0243; HI4PI Collaboration et al. 2016). We do not

have strong constraints on the X-ray emission before that date, although from the archival MAXI observations (black triangle upper limits) we can rule out X-ray emission with the same luminosity and lightcurve of the jetted TDE Sw J1644 (red line). We cannot rule out a flare with average luminosity over $\sim$100 days that is $\lesssim 2 L_{\mathrm{edd.}}$.

The late-time X-ray spectrum is shown in Figure 4. We used `xspec` to fit the X-ray emission to an absorbed power law (`cflux*TBabs*zTBabs*powerlaw`) and a blackbody (`cflux*TBabs*zTBabs*bbody`).In both cases, we include both Milky Way extinction, for which we fix the hydrogen column density to the known value $N_{H,\mathrm{MW}} = 1.52 \times 10^{20}$ cm^{-2} (HI4PI Collaboration et al. 2016), and intrinsic extinction, for which we let the Hydrogen column density float. The best-fit models are shown in Figure 4. The pure blackbody cannot fit our observations (`cstat`/dof = 195/32), but power law (`cstat`/dof = 33.7/33) provides a statistically acceptable fit. The best-fit power law parameters are: intrinsic column density $< 7.7 \times 10^{19}$ cm^{-2} (5σ), photon-index $\Gamma = 2.98 \pm 0.06$, and an absorbed $0.3 - 10$ keV flux density $\log f_{0.3-10\,\mathrm{keV}} = -12.86 \pm 0.01$ ($L_{0.3-10\,\mathrm{keV}}/(\mathrm{erg\,s}^{-1}) = 42.3 \pm 0.01$). We will discuss the interpretation of these parameters later in this section.

We consider three general categories of X-ray sources: (1) star formation in the host galaxy, (2) an accretion disk with or without a hot electron corona, (3) other transient emission associated with VT J2043. We will now discuss the likely contribution of each of these sources in turn.

X-ray photons associated with star formation are predominantly emitted by low- and high-mass X-ray binaries (LMXBs/HMXBs; Mineo et al. 2014). The star formation rate is correlated with the $2 - 10$ keV X-ray luminosity as SFR$= (1.40 \pm 0.32) \times \frac{L_{2-10\,\mathrm{keV}}}{10^{40}\,\mathrm{erg\,s}^{-1}} M_\odot$ yr^{-1} (Vattakunnel et al. 2012). To reproduce the observed $2 - 10$ keV luminosity of 4.7×10^{40} erg s^{-1}, we require that the SFR$= 6.58 \pm 1.5 M_\odot$ yr^{-1}. This is consistent with our SED fit, but our SED fit provides very weak constraints on the SFR. It is also consistent with our pre-flare radio limits: radio emission due to star formation has been empirically measured to be SFR$= 5.52 \times 10^{-22} L_{1.4\,\mathrm{GHz,SFR}}$ for $L_{1.4\,\mathrm{GHz,SFR}} > 6.4 \times 10^{28}$ erg s^{-1} Hz^{-1}, which corresponds to $L_{1.4\,\mathrm{GHz,SFR}} =$
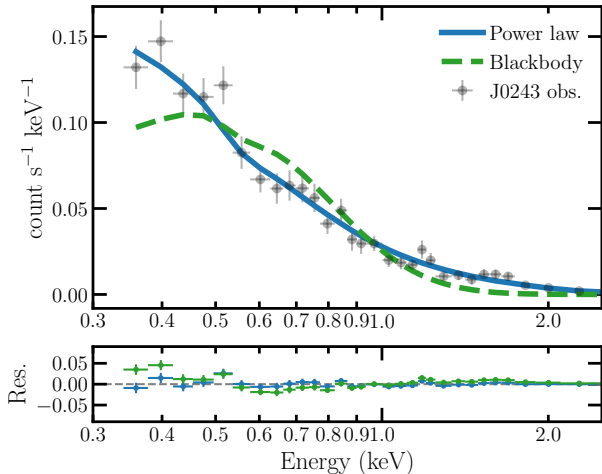
Figure 4. The *XMM*-Newton x-ray spectrum for 2dFGRS TGS314Z138. The observations are the black points, while the lines show model fits. The emission is most consistent with a power law model with little intrinsic hydrogen column density.

0.83 ± 0.22 mJy for SFR$= 6.58 \pm 1.5$. This star formation rate is inconsistent with the observed Hα emission: from Section 4.1, the SFR based on the Hα emission is SFR$= 0.56 \pm 0.16$. This expression for the SFR-Hα correlation is only valid if the SFR has been $\sim$ constant for > 6 Myr, but, if the star formation was very recent, we would not expect to see the X-ray emitting LMXBs and HMXBs. Hence, it is unlikely the X-ray emission was produced by star formation. We briefly consider alternative X-ray sources in the rest of this section.

X-ray emission from AGN is dominated by thermal emission from the disk, and inverse Comptonized thermal photons by the hot electron corona (Haardt & Maraschi 1991). Using the observed correlation between narrow [O III]λ5007 and Hα with X-ray luminosity (Netzer et al. 2006), an accretion disk can account for all of the observed X-ray flux. Given that the X-ray lightcurve is consistent with a constant luminosity, it is feasible that the X-ray emission is entirely due to an active accretion disk. A $\Gamma \sim 3$ power law spectrum is consistent with observations of narrow line Seyfert 1 galaxies (Grupe et al. 2010), although radio-loud Seyferts typically have flatter X-ray spectra ($\Gamma \sim 2$; Komossa 2018), but with large scatter.

The X-ray emission from 2dFGRS TGS314Z138 is not entirely consistent with "normal" Seyferts. The intrinsic column density is consistent with zero and inconsistent with the $n_{\mathrm{H}} > 10^{22}$ cm^{-2} typically measured in Seyfert 2s (Risaliti et al. 1999). For standard AGN, such a low gas column density means that the BLR should be observable (Panessa & Bassani 2002). However, as

discussed in Section 4.1, we do not detect any broad line emission. This low n_{H} may support the hypothesis that the X-ray emission is dominated by star formation. If it is not, and the column density is truly near-zero, 2dFGRS TGS314Z138 may be a "true" Seyfert 2, which show small X-ray column densities but no broad line emission (Hawkins 2004).

Finally, we consider the scenario where the observed X-rays are transient, rather than associated with an old accretion disk or star formation, and consider a few of the possible origins. X-rays may be emitted from the forward shock of the outflow, as may have been the case for jetted TDEs like Sw J1644+57 (Eftekhari et al. 2018). In this case, we expect the X-ray slope to be $\Gamma = p/2 + 1 = 2.1 \pm 0.05$, where p is taken from Table 3. This Γ is significantly inconsistent with our measured value. bremmstrahlung associated with the electrons in the radio-emitting outflow and dense clumps of CNM gas could produce X-rays, but we would expect a harder power-law spectrum in this case.

The X-rays may be associated with a new corona and associated accretion disk, formed as a result of, e.g., a stellar disruption. The observed power-law spectrum would be consistent with expectations for a transient corona/disk (Osterbrock 1991).

In summary, VT J0243 is not associated with an extraordinarily bright X-ray flare as has been observed for the extremeley luminous, on-axis, jetted TDEs. We cannot rule out a flare with $L \lesssim 2L_{\mathrm{edd.}}$. VT J0243 is detected in late-time X-ray observations with a $0.3-10$ keV luminosity $L_X \sim 10^{42.3}$ erg s^{-1}, photon index $\Gamma \sim 3$, and negligible intrinsic column density. This emission is unlikely to be related to star formation. Instead, it is most likely a transient, or a pre-existing accretion disk.

4.4. *Infrared and optical analysis*

In Figure 1, we show the infrared (bottom) and optical (middle) light curves for VT J0243. In this section, we will provide brief analyses of the possible origins of the observed transient emission. Because of the low cadence and insufficient sensitivity of the observations, we will not perform any detailed modelling.

There is a significant flare detected by the PanSTARRS survey near MJD$\sim$55895 with g-band luminosity $L_g \sim 4 \times 10^{42}$ erg s^{-1}. The flare brightened and faded over a timescale smaller than the PanSTARRS cadence ($\lesssim 400$ days). Given the low cadence, we cannot measure light curve shape in more detail, but it is consistent with optically-detected TDEs, which typically rise over tens of days and fade over $\sim$60 days (van Velzen et al. 2021). The co-temporal CRTS observations detect the flare at a $\sim$2σ level but are not sensitive enough to reliably constrain the lightcurve. They do suggest that the flare peaked around the time of the brightest PanSTARRS observation, so the peak luminosity is likely within a factor of a few of $L_g \sim 4 \times 10^{42}$ erg s^{-1}. This is slightly dimmer than but consistent with typical

optically-detected TDEs; the dimmest TDE from van Velzen et al. (2021) peaked at $L_g \sim 7 \times 10^{42}$ erg s^{-1}. We fit the fluxes to a blackbody assuming no intrinsic extinction, which is reasonable given the low column density measured from the X-ray spectrum (Section 4.3).

The optical fluxes at peak are consistent with a blackbody with no extinction and temperature $\log T_{\rm bb}/{\rm K} = 4.35 \pm 0.38$ and radius $\log R_{\rm bb}/{\rm pc} = -3.89 \pm 0.34$, corresponding to a blackbody luminosity $\log L_{\rm bb}/({\rm ergs}^{-1}) = 43.4 \pm 1.7$. Again, these blackbody parameters are all standard for optically-detected TDEs. We cannot rule out that the flare has repeated. Shortly after the peak, the optical emission rebrightens slightly to $L_g \sim (6.7 \pm 1) \times 10^{42}$ erg s^{-1}. The fluxes at the rebrightening are consistent with a blackbody with no extinction and temperature $\log T_{\rm bb}/{\rm K} = 3.70 \pm 0.07$ and radius $\log R_{\rm bb}/{\rm pc} = -3.19 \pm 0.20$, corresponding to a blackbody luminosity $\log L_{\rm bb}/({\rm ergs}^{-1}) = 42.3 \pm 0.5$. This blackbody luminosity is roughly an order of magnitude fainter than the brighter peak. The temperature is significantly cooler than the first peak, and the emission may come from a larger radius.

Unfortunately, because of the limited cadence of the PanSTARRS observations and the large uncertainties even at the optical peak, we cannot perform detailed modelling to determine the origin of the optical flare. The peak emission can be modelled as a standard accretion disk. It also could be a thermally-emitting outflow, heated by EUV emission from, e.g., an accretion disk, as may be observed in TDEs.

The infrared lightcurve shows variability with an approximate amplitude $\sim 150\,\mu$Jy ($\sim 10^{42}$ erg s^{-1}). The emission appears to redden slightly between the first three epochs and the rest of the MIR observations, which suggests that the MIR-emitting dust was heated when, e.g., the accretion rate increased. Intriguingly, the time period when this change must have occurred is roughly consistent with the range of launch dates constrained by the outflow radius evolution, and the time of the optical flare. The average change in flux density in each band between the first three epochs and the later observations is $\Delta f_\nu({\rm W1}) = 44.8 \pm 11.1\,\mu$Jy, $\Delta f_\nu({\rm W2}) = 88.5 \pm 17.6\,\mu$Jy, where the uncertainties are determined through the standard deviation of the observations.

If we assume that the dust started out cold and the entire flux change was due to the dust heating, we can fit the Δf_ν values during each WISE epoch to a blackbody to estimate the dust temperature and luminosity, albeit with large uncertainties and covariances. The average temperature over all WISE epochs is 865 ± 259 K and the bolometric luminosity $\log L_{\rm IR}/({\rm erg\,s}^{-1}) \sim 41.69 \pm 0.15$. If we assume dust with a covering fraction ~ 1, this implies it is located at an unrealistically small radius $\sim 10^{-2}$ pc. Instead, we favor a scenario where more distant dust with a low covering fraction is located farther away (e.g., a covering fraction $\sim 1\%$ corresponds to a distance ~ 0.1 pc). Low covering fractions of $\sim 1\%$

are consistent with measurements from IR flares during TDEs in quiescent galaxies (Jiang et al. 2021). AGN typically have high covering fractions $\gtrsim 40\%$ due to the dusty torus (e.g. Ricci et al. 2017). The best fit average dust luminosity suggests that the bolometric luminosity of the EUV flare that heated the dust was $\log L_{\rm EUV}/{\rm erg\,s}^{-1} \sim 43.2 - \log(\frac{f_{\rm cov,dust}}{1\%})$. Unless the dust covering fraction is abnormally small, the EUV flare was sub-Eddington ($\lesssim 1\% L_{\rm edd.}$).

This analysis of the IR flare assumes that there was no emission in between the low cadence WISE observations. A higher Eddington ratio EUV flare could have heated the dust between the IR observations, and we would not observe it. Hence, these constraints should be taken with a large grain of salt.

In conclusion, the low amplitude of the WISE variability suggests that either this galaxy has an extraordinarily low dust covering fraction, even when compared to completely quiescent galaxies, or that any EUV flare in the time period under question was sub-Eddington. There may have been a higher luminosity EUV flare in between the WISE observations. Moreover, this analysis has been subject to many poorly supported-assumptions. For example, if there was pre-existing accretion disk, our assumption that the dust was initially cold would be incorrect.

5. DISCUSSION

The radio emission associated with VT J0243 is likely caused by the launching of a jet. Sub-relativistic outflows never produce the observed high luminosity radio emission ($\nu L_\nu(3\,{\rm GHz}) > 10^{40}$ erg s^{-1}), nor such high energies ($E \sim 10^{51}$ erg). Even fast ($\beta > 0.1$), wide angle outflows from AGN are generally associated with radio-quiet sources and are compact ($\lesssim 0.1$ pc). Such outflows are not expected to be produced by disks with very low accretion rates, and no outflow has ever reproduced the observed outflow velocity, radio luminosity, and radio/X-ray luminosity ratio. Hence, we do not consider wide-angle, non- or semi-relativistic outflows further. Instead, we assume VT J0243 is associated with the launching of a jet. In this section we discuss the answer to the question: why did a jet launch? First, we summarize our observations:

- X-ray emission with $\log L_X/{\rm erg\,s}^{-1} = 42.3 \pm 0.01$ and a power-law spectrum with index $\Gamma = 2.98 \pm 0.06$ and a column density consistent with the Milky Way value. The emission is likely associated with a hot accretion disk and electron corona. The emission may have been transient or persistent, and may have evolved over the last few decades. The peak luminosity was likely $\lesssim 2 L_{\rm edd.}$.

- Transient radio emission with a current luminosity $\nu L_\nu(5\,{\rm GHz}) = 3.6 \times 10^{40}$ erg s^{-1}. The radio-emitting outflow is currently at a radius
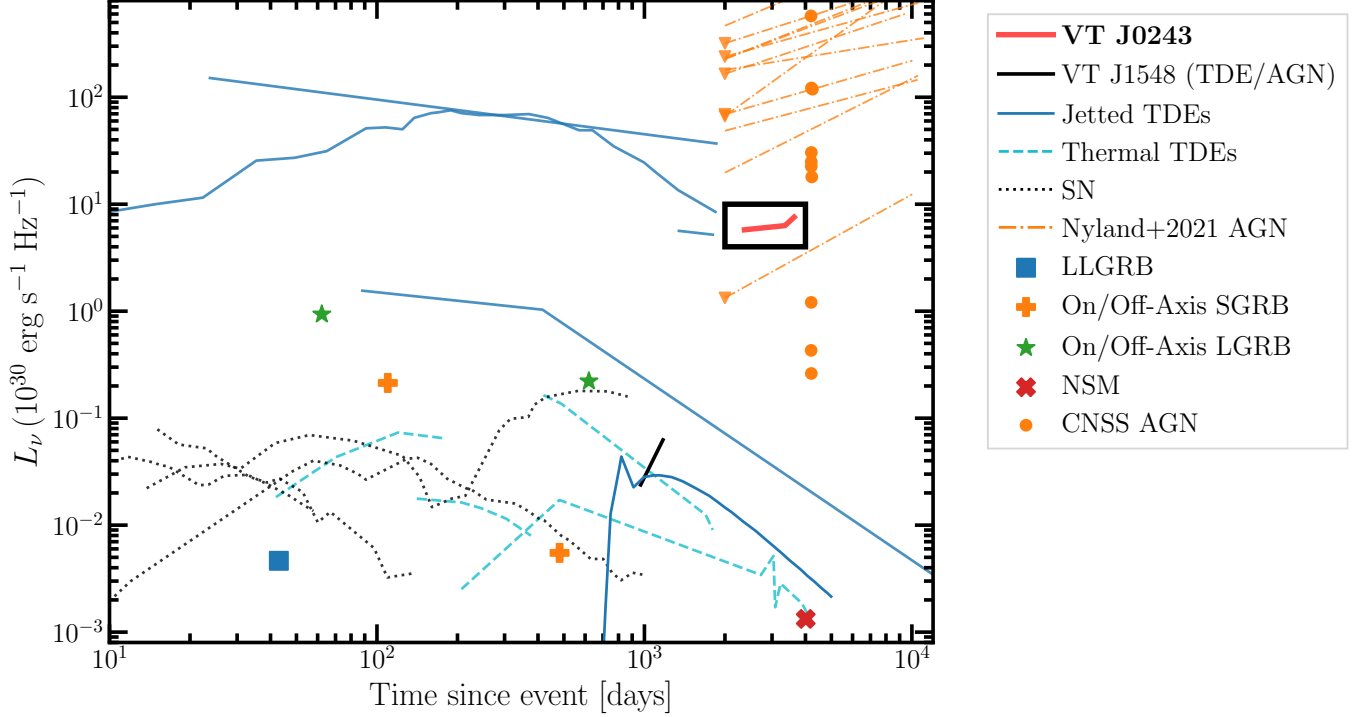
Figure 5. Radio light curves (lines) and typical durations/luminosities (squares) for classes of radio transients. The squares are retrieved from Metzger et al. (2015) and are measured at 1.4 GHz. The TDE lightcurves are from Alexander et al. (2020); Ravi et al. (2021); Mattila et al. (2018), and references therein, and are largely at 5 GHz. The SN lightcurves are at $5 - 8$ GHz, are from Salas et al. (2013); Soderberg et al. (2006, 2010); Kulkarni et al. (1998). The lightcurve for VT J1548 is measured at 3 GHz Somalwar et al. (2021). For comparison, the 5 GHz lightcurve of VT J0243 is shown in red, assuming the flare was launched around MJD 56000. This source is of comparable brightness to jetted TDEs, but is still rising whereas previous events began fading by $\sim$1000 days post-event. It is also at a comparable luminosity to the newly radio loud AGN from Wołowska et al. (2021), shown as orange circles, and the radio variable AGN from Nyland et al. (2020), which are shown as orange dot-dashed light curves. The triangles in the light curves denote upper limits. We have arbitrarily chosen the start date of these AGN flares for ease of comparison to VT J0243.

$R = 0.71 \pm 0.02$ pc. It has an average velocity $0.1 < \beta < 0.6$, or $1.005 < \Gamma < 1.3$, and is currently non-relativistic. It has a high equipartition energy $\sim 10^{52}$ erg and a moderate electron density, $\gtrsim 1$ cm^{-3}, depending on the assumed fraction of the energy stored in the magnetic field. The magnetic field is $\sim 10^{-2}$ G.

- Significant optical variability, peaking at $L_g = 4 \times 10^{42}$ erg s^{-1}. The flare peaks around MJD 56000, and fades over $\lesssim$400 days. The peak is consistent with a $T \sim 2 \times 10^4$ K blackbody with bolometric luminosity $10^{43.4}$ erg s^{-1}. After the flare faded, it rebrightened to a cooler blackbody ($T \sim 5000$ K) with a bolometric luminosity an order of magnitude dimmer at $10^{42.3}$ erg s^{-1}.

- Weak MIR variability suggesting that any EUV flare in the last $\sim$5000 days was sub-Eddington, unless it occured between the low cadence IR ob-

servations. The MIR variability increased around MJD 56000, which is consistent with the launch date of the radio-emitting outflow if the outflow has travelled at a constant β.

- The host galaxy of VT J0243, 2dFGRS TGS314Z138, shows narrow line emission consistent with historic, weak Seyfert activity. The MIR colors, on the other hand, are consistent with quiescent galaxies.

In the rest of this section, we consider the possibility that this source is caused by a nascent jet associated with an accreting black hole. First, for completeness, we briefly discuss, and rule out, an alternate possibility: a supernova-triggered jet.

5.1. *Supernova-triggered jet*

Supernovae (SNe) can produce radio emission spanning from $L_\nu \sim 10^{25-32}$ erg s^{-1} Hz^{-1} for timescales

as long as ten years (Weiler et al. 2002; Mooley et al. 2016). The emission is often synchrotron emission associated with an outflow/jet colliding with the dense, local environment or a relativistic jet (e.g. Chevalier 1998; Soderberg et al. 2010). Typical SNe do not remain as bright as VT J0243 for such long periods of time (see Figure 5). Moreover, the $\mathcal{O}(\mathrm{pc})$ size of the radio emitting outflow/jet associated with VT J0243 would be highly unusual. A gamma-ray burst (GRB) can produce such an outflow; however, no GRB has been observed with a rising radio luminosity thousands of days post-explosion (e.g. Kangas & Fruchter 2021). Moreover, the observation of $\nu_{\mathrm{sa}} < \nu_m$ thousands of days post-explosion is inconsistent with models of GRB outflow evolution (Granot & Sari 2002). Hence, VT J0243 is unlikely to be related to a supernova.

5.2. Black hole accretion-triggered jet

Accreting black holes, whether stellar mass or supermassive, are well established to be associated with jet activity. The process through which the jet is launched, the connection between the accretion disk and the jet, and the connection between the black hole properties (i.e., spin) and the jet remain open questions. In the following sections, we provide a basic summary of the physics of jets associated with black holes and accretion, and then we compare the properties of VT J0243 to those expected for young jets launched from accreting black holes.

While the stellar mass black hole regime is not relevant to VT J0243, our understanding of jet physics and the disk-jet connection for stellar mass black holes is more sophisticated. We are better able to study these events because of the short timescales associated with the disk and jet evolution, which allow real-time observations of the jet and disk life cycles, and the smaller dynamic ranges of the systems, which allow for more realistic simulations. Ideally, the accretion disk and black hole evolution would be scale-free, so we can apply the same physics to stellar mass black holes and SMBHs. In reality, effects such as the mass-dependence of the inner disk temperature introduce a scale-dependence (e.g. Fender et al. 2007). These effects have critical effects on accreting SMBHs, causing them to behave very differently in certain regimes (e.g., at very high accretion rates) from XRBs. Despite this, much of the stellar mass black hole physics is relevant to SMBHs, so we begin with a summary of stellar mass black hole disc/jet evolution. Then, we discuss the SMBH regime, and finally focus the discussion to comparisons with VT J0243.

5.2.1. X-ray binary disk-jet connection

The evolution of accreting stellar-mass black hole systems, X-ray binaries (XRB), is best understood by considering the evolution in X-ray hardness/luminosity space. When the X-ray binary is extremely sub-Eddington ($L_X/L_{\mathrm{edd.}} < 0.01$), the X-ray emission is low, with a flat spectral slope. Hence, this is called the low-hard state. In this low Eddington ratio regime, the accretion disk is geometrically-thick, optically-thin, and hot. It is radiatively inefficient, so advection dominates and this type of disk is called an advection dominated accretion flow (ADAF; Narayan & Yi 1994). In the low-hard state, the XRB is typically observed to have a mildly relativistic ($\Gamma < 2$) jet (Fender et al. 2004).

As the Eddington ratio increases, the X-ray luminosity increases but the spectrum remains hard as the ADAF continues to dominate the disk. The radio luminosity likewise increases. Eventually, the X-ray emission reaches a peak, as the high Eddington ratio has caused the geometrically-thin outer-disk to extend into the inner disk and replace the ADAF. The X-ray spectrum softens, while the luminosity remains roughly constant (Fender 2010). During this softening, the jet Lorentz factor increases to $\Gamma > 2$, and the jet emission becomes intermittent and dominated by discrete blobs (Fender 2010). Soon after this change in the jet properties, the XRB will pass the "jet line", which is a characteristic hardness ratio at which the steady jet completely vanishes (Fender et al. 2009). The XRB is now in the high-soft state. After this stage, the Eddington ratio will drop while the spectrum remains soft. At low Eddington ratios, the ADAF will begin to dominate again and the X-ray hardens. The XRB will cross the jet line again, and a new jet will launch.

The processes through which the jet is quenched and launched are not fully understood. Both likely involve changes in the magnetic field in the accretion disk. The jet is likely collimated by pressure from external material; hence, the prevalence of jets in low Eddington ratio AGN with puffy disks (Tchekhovskoy et al. 2010). The internal jet magnetic fields are generally unable to collimate more than the extreme base of the jet (Tchekhovskoy et al. 2009). As we will discuss in Section 5.2.4, jets are also sustainable near SMBHs accreting at near- or super-Eddington rates, as the disk again becomes puffy and the jet can be collimated.

XRBs largely remain in the quiescent low-hard state, only entering the high-soft state during outbursts that are thought to be triggered by instabilities in the accretion disk (Fender 2010). There is some evidence that black hole spin is positively correlated with jet power, as would be expected if jets are powered by the Blandford & Znajek (1977) mechanism. However, the sample of XRBs with known spins remains small (Fender et al. 2010).

5.2.2. The disk-jet connection for supermassive black holes

There is observational evidence that the disk-jet connection for XRBs can be extrapolated to accreting SMBHs. For example, there is a tight, black-hole-mass dependent correlation between the X-ray and radio luminosities of XRBs, and observations of AGN have shown that these SMBHs lie on the same correlation

(Gültekin et al. 2019). Moreover, a modified version of the X-ray hardness-luminosity diagram, which replaces the X-ray hardness with the relative luminosity in power law and disk blackbody components, shows the same structure for XRBs and AGN (Fender 2010). It is not clear, however, that AGN follow the same cycle as XRBs in this diagram. The disk instabilities that cause XRB outbursts have not been proven to occur in AGN (Janiuk & Czerny 2011). The relationship between spin and jet power is observationally unclear, as for X-ray binaries. The observed dichotomy between the radio-loud and quiet low-luminosity AGN (LLAGN) populations ($\sim$10% of LLAGN are radio loud) is plausibly explained if the radio-quiet LLAGN have low SMBH spins while the radio-loud sources have extremal spins (Tchekhovskoy et al. 2010). AGN simulations unambiguously find a strong, positive correlation between jet power and spin (Tchekhovskoy et al. 2010).

As with XRBs, AGN with lower Eddington ratios ($\ll 0.1$) often have weak jets (Falcke et al. 2001; Fabian 2012; Laha et al. 2021). As we will discuss in Section 5.2.4, there is strong evidence that accreting black holes at near- or super-Eddington rates also launch jets. For example, the TDE Sw J1644 launched a powerful jet during a period of near- or super-Eddington accretion. The exact mechanism through which this jet was launched is unconfirmed, but the observation of a jet from such a young accreting system suggests that the accretion disk became strongly magnetized remarkably quickly (Tchekhovskoy et al. 2014).

In summary, one can draw parallels between the high-soft/low-hard classification for XRBs and the observed states of AGN, although there are many differences. For example, AGN do not cycle between the high-soft/low-hard states during disk instability-driven outbursts like XRBs, and the mechanism that causes AGN to perform this transition (with its associated jet quenching/launch) is unknown. There may be a correlation between SMBH spin and jet power, although this is not observationally confirmed.

With this background in the jet-disk connection and the factors that control the launching of a SMBH jet, we now turn towards VT J0243. We consider two scenarios. First, VT J0243 may be a young jet launched from a system that has been actively accreting since long before the jet was launched, i.e., an AGN. Alternatively, VT J0243 may be a jet launched near the onset of accretion. In this case, much of the previous discussion must be altered, as the properties of very young accretion disks are distinct from old disks (in particular, the magnetizations). The combination of young accretion and a new jet is expected for TDEs, so we discuss the possibility that VT J0243 is a jetted TDE.

5.2.3. *VT J0243 as a young jet from an AGN*

First, we consider the possibility that VT J0243 is a young jet from an AGN. We briefly compare the observations to the theory summarized in the previous subsections, and then we perform a detailed comparison of the observations of VT J0243 and known, young AGN jets.

From a theoretical perspective, even if all of the X-ray emission is due to an accretion disk/corona, VT J0243's bolometric luminosity is sufficiently low that it is feasible that we are observing an AGN in the low-hard state that has launched a jet. The lack of dust, based on the infrared colors and X-ray absorption, and the low luminosities inferred from the IR and optical observations support the hypothesis that any pre-existing accretion disk was in a low state. The low average bulk Lorentz factor of the outflow ($\Gamma < 1.3$) is also consistent with the $\Gamma < 2$ jets typically associated with this state.

Of course, we cannot exclude that this event had an Eddington ratio $\gtrsim$0.1 during the jet launching, although the infrared observations and X-ray limits constrain the Eddington ratio to $\lesssim 1$. If the Eddington ratio is $\gtrsim$0.1 but not near- or super-Eddington, VT J0243 is in a regime where the physics of jet activity is very unclear. As we have discussed, in XRBs these higher Eddington ratios are associated with no jet activity. However, AGN in this regime are observed to be radio loud, and the mechanism through which the radio-emitting jet is produced is not fully understood (see Liska et al. 2021 for simulations of a thin accretion disk that can support jet activity).

VT J0243 is consistent with theoretical expectations, albeit with uncertainties due to the unknown Eddington ratio at the time of jet launch. To further constrain the origin of VT J0243, we compare its properties with past observations. First, we compare the properties of VT J0243 and its host to the population of *persistent* radio-loud Seyferts. Later, we will focus back to transient sources and young jets.

Astronomers have discovered jetted Seyfert galaxies, like VT J0243, although they are uncommon. Around $\sim$15% of broad line AGN are very radio-loud, where radio loudness is measured by the parameter $R_{\mathrm{RL}} = f_{6\,\mathrm{cm}}/f_{4400\,\mathrm{\AA}}$ and $R_{\mathrm{RL}} > 100$ is the cut for very radio-loud AGN (Komossa et al. 2006). In contrast, only $\sim$2.5% of Seyfert 1s have $R_{\mathrm{RL}} > 100$, so these galaxies tend to be radio quiet (Komossa et al. 2006). Radio loud Seyferts may have high black hole masses $\sim10^{7-8}\,M_\odot$ compared to the general Seyfert population, but still much lower masses than general radio-loud AGN ($\sim10^9\,M_\odot$) (Komossa et al. 2006). These black hole masses for radio-loud Seyferts are still higher than observed for VT J0243. Radio-loud Seyferts also have flat X-ray spectra ($\Gamma \sim 2$ for radio-loud Seyferts compared to $\Gamma \sim 2.9$ for the general Seyfert population) with rapid variability on as short as hour timescales (Komossa 2018). Note that the typical X-ray spectral slopes of radio-loud Seyferts are shallower than that of VT J0243. Radio-loud Seyferts have high Eddington

ratios, and show strong Fe II emission, both in contrast. Finally, ~70% of radio-loud Seyferts show compact, steep radio SEDs, analogous to the more general compact, steep spectrum (CSS) source population. This compact emission suggests an overabundance of young radio-emitting jets, which do not form into ~kpc scale structures like observed in FR I/II galaxies (Berton et al. 2020). In summary, the population of persistent radio-loud Seyferts shows some similarities to VT J0243, but many distinctions.

VT J0243 is not a persistent source, of course. Candidate young radio jets in AGN and Seyferts have become more common in recent years. Mooley et al. (2016) reported an AGN that switched from radio-quiet to radio-loud on a decade timescale, and more recently, Kunert-Bajraszewska et al. (2020) and Wołowska et al. (2021) published the first samples of such objects. We show individual light curves for these turning-on radio AGN in Figure 5. VT J0243 has a luminosity and timescale consistent with these events.

Likewise, VT J0243 is consistent with observations of the jet power and bolometric luminosity of young, radio-loud AGN, which occupy specific regions of jet power−bolometric luminosity parameter space (Wołowska et al. 2021). Adopting $P_J = 5 \times 10^{22}(L_{1.4\,\mathrm{GHz}}/\mathrm{W\,Hz^{-1}})^{6/7}$ erg s^{-1} (Rusinek et al. 2017), and using the X-ray luminosity to approximate the bolometric luminosity with a bolometric correction factor ~20 (Lusso et al. 2012), we find $P_J \sim 10^{43.2}$ erg s^{-1} and $L_{\mathrm{bol}} \sim 10^{43.6}$ erg s^{-1} ~ $0.046 L_{\mathrm{edd}}$ for VT J0243. This low Eddington ratio places the source slightly above the border of the radiatively inefficient regime, where most of the AGN energy is channeled into a radio-emitting jet. This regime is typically defined as $L_{\mathrm{bol}}/L_{\mathrm{edd.}} \lesssim 10^{-2}$. Given the large uncertainties in the bolometric luminosity of VT J0243, as discussed previously, we cannot convincingly place VT J0243 on either side of this dividing line. If we adopt $L_{\mathrm{bol}}/L_{\mathrm{edd.}} \sim 10^{-1.3}$ and $P_J/L_{\mathrm{bol}} \sim 10^{-0.4}$, we find VT J0243 is consistent with radio-detected AGN (Wołowska et al. 2021).

On the other hand, VT J0243 has a unique radio SED relative to typical young jetted AGN. Young radio jets from AGN are observed to fall on a characteristic line in peak frequency−linear size parameter space (e.g. Nyland et al. 2020). VT J0243 has a significantly smaller linear size compared to other young radio-loud AGN with the same peak frequency, which are typically hundreds of parsec in size.

Even if we only consider Seyferts, VT J0243 has unusual radio SED properties. A few expamples of bright radio flares from Seyferts have been detected. Lähteenmäki et al. (2018) observed 66 radio-quiet, narrow line Seyfert 1 galaxies at 37 GHz, and detected eight. These sources were undetected in archival observations from the VLA Faint Images of the Radio Sky at Twenty-Centimeters (FIRST) survey. They show variability at 37 GHz as large as a Jansky and on month−year

timescales. Seyferts can produce bright radio flares. In contrast to VT J0243, the low frequency emission from these Seyferts is weak (~micro-milliJy), suggestive of strong absorption at low frequencies (Berton et al. 2020).

In summary, while VT J0243 may be consistent with expectations for a young jetted AGN from a theoretical perspective, its radio SED is distinct from typical young jetted AGN, it has a soft X-ray spectrum, and its host properties are unusual. For example, it has quiescent host IR colors, a lack of strong evidence for ongoing AGN activity within a few thousand years of the radio flare, and a low black hole mass. Given the large range of properties of young jetted AGN and the large theoretical uncertainties, we do not rule out that we are observing such an event. However, if VT J0243 is a young jetted AGN, it is an extremely unusual member of this class.

5.2.4. *VT J0243 as a young jet from a TDE*

Tidal disruption events (TDEs) occur when a star ventures within the tidal radius, $R_T \sim R_*(M_*/M_{\mathrm{BH}})^{1/3}$, of a nearby SMBH (e.g. Frank & Rees 1976; Rees 1988; van Velzen et al. 2011; Donley et al. 2002). The bulk of TDEs are "thermal" TDEs with $\nu L_{\nu,\mathrm{GHz}} \lesssim 10^{38}$ erg s^{-1}, which are dominated by a thermally-emitting, hot accretion disk in the soft X-ray, and its reprocessed emission at lower energies (Alexander et al. 2020). The radio emission mechanism for thermal TDEs is poorly constrained, but may be associated with a disk wind or stellar debris outflow that is colliding with the CNM (Alexander et al. 2020). As is clear from Figure 5, VT J0243 is much brighter than all known thermal TDEs.

The luminosity of VT J0243 is, however, consistent with the jetted TDE population, which includes the three brightest ($\nu L_{\nu,\mathrm{GHz}} \gtrsim 10^{40}$ erg s^{-1}) of the ~20 radio-detected TDEs (Cenko et al. 2012; Pasham et al. 2015; Brown et al. 2017; Zauderer et al. 2011; Berger et al. 2012; Wiersema et al. 2020; Zauderer et al. 2013; Yang et al. 2016; Eftekhari et al. 2018). The radio properties of these events are best exemplified through Sw J1644+57, the earliest example of an on-axis, jetted TDE. Sw J1644+57 was discovered by the *Swift* Burst Alert Telescope in 2011, and was promptly observed by a variety of telescopes across the electromagnetic spectrum. Within a few days, a radio outflow was detected at a luminosity near 10^{40} erg s^{-1} and best-modelled as relativistic ($\Gamma \sim 3$) with $\nu_{\mathrm{sa}} < \nu_m$. The energy in the outflow increased over ~300 days from ~2×10^{50} erg to ~4×10^{51} erg while Γ decreased as ~$t^{-0.2}$. $\gtrsim 300$ days post-launch, the energy plateaued, the peak flux began decreasing, and the SED transitioned to the regime with $\nu_{\mathrm{m}} < \nu_{\mathrm{sa}}$. The outflow transitioned to non-relativistic motion ~700 days post-launch.

Around the same time as the radio turned-on, Sw J1644+57 exhibited a bright X-ray flare peaking at an isotropic luminosity ~10^{48} erg s^{-1}, which is ~$2 - 3$ orders of magnitude brighter than the Eddington luminosity of the SMBH. The X-ray emission declined as ~$t^{-5/3}$,

corresponding to the mass fallback rate during a TDE, and showed strong variability on < 1 day timescales. At 500 days post-launch, the X-ray emission plummeted precipitously to $L_X \sim 10^{36}$ erg s^{-1}, which has been interpreted as the jet turning off. Because the X-ray luminosity tracks the expected mass fall back rate after a TDE, it is thought to be powered by a mechanism closely tied to the jet. Crumley et al. (2016) comprehensively surveyed many possible mechanisms, and favored models in which the X-ray photons are produced through either synchrotron emission or inverse-Comptonization of external photons (i.e., off the accretion disk). The emitting electrons are likely accelerated by magnetic reconnection in a Poynting flux-dominated jet. In this case, the fact that the observed jet was on-axis allowed the X-ray emission to be beamed, enabling the extremeley high luminosities observed.

In contrast to Sw J1644+57, and other similar events, VT J0243 is not associated with hugely super-Eddington X-ray flare. Only one other jetted TDE candidate was not detected as a bright X-ray transient, and this event was off-axis and in the highly obscured nucleus of a merging galaxy. VT J0243 may also be an off-axis jetted TDE. If we assume VT J0243 is a jetted TDE, this suggests that there will be a population of such events that cannot be detected via, e.g., X-ray transient surveys, but require wide field, deep radio surveys like VLASS.

VT J0243 also differs from Sw J1644+57-like events in its radio lightcurve. The ~ 5 GHz luminosity is still increasing > 1000 days post-launch, whereas "typical" jetted TDEs have long since begun fading at similar frequencies. Moreover, at > 1000 days post-launch the SED is still in the regime where $\nu_{\rm sa} < \nu_m$. These observations may suggest that the jet has yet to turn off. Unusually slowly evolving TDEs are not unprecedented: some observed non-jetted TDEs evolve on much slower timescales than expected (see Somalwar et al. 2021 Section 7.1 and references therein). The timescale of a TDE depends on factors including the stellar orbital parameters, the stellar structure, and the energy dissipation rate of the tidal debris. We may be seeing the jetted analogue of events in a regime with, e.g., a low energy dissipation rate, such that the accretion disk formation is delayed and the evolution slowed. In the case of VT J0243, the jet launch may have been enabled by magnetization provided by a fossil accretion disk, as was proposed in the case of Sw J1644+57 (Tchekhovskoy et al. 2014).

In summary, VT J0243 is plausibly a jetted TDE. However, it differs from known jetted TDEs because of the slow timescale of the radio evolution and lack of an X-ray counterpart, the latter of which may support the idea that we are observing an off-axis jet.

6. CONCLUSION

We have presented an extraordinarily bright and long lasting radio flare in a galactic nucleus detected in the VLA Sky Survey. VT J0243 rose to $\sim 10^{40}$ erg s^{-1} in a time period of $\sim 5 - 20$ years. Radio follow-up suggests the presence of a compact, relativistic jet. X-ray emission with a luminosity $L_X = 10^{42.3}$ erg s^{-1} is observed, which may be associated with a pre-existing or transient corona and accretion disk. Faint IR variability and an $L_g = 10^{42}$ erg s^{-1} optical flare are observed, both consistent with reprocessed emission from a sub-Eddington EUV flare. VT J0243 is hosted by a weak Seyfert galaxy. A more detailed summary of our observations is provided at the beginning of Section 5.

VT J0243 is a unique example of a young radio source. It is likely caused by the launch of a powerful jet, combined with strongly sub-Eddington multiwavelength flares. This is consistent with a tidal disruption event, although the TDE likely evolved very slowly. It may also be an AGN, but the trigger for the abrupt accretion enhancement is unknown. In either case, VT J0243 highlights the complicated connection between SMBH accretion and jet launching. In the near future, radio surveys like VLASS will hopefully uncover large populations of similar, nascent jets, which, combined with extensive multiwavelength follow-up as was performed in this work, will illuminate the true triggers of such dramatic radio flaring and their connection with SMBH activity.

REFERENCES

Alexander, K. D., van Velzen, S., Horesh, A., & Zauderer, B. A. 2020, SSRv, 216, 81, doi: 10.1007/s11214-020-00702-w

Assef, R. J., Stern, D., Noirot, G., et al. 2018, ApJS, 234, 23, doi: 10.3847/1538-4365/aaa00a

Baldwin, J. A., Phillips, M. M., & Terlevich, R. 1981, PASP, 93, 5, doi: 10.1086/130766

Barniol Duran, R., Nakar, E., & Piran, T. 2013, ApJ, 772, 78, doi: 10.1088/0004-637X/772/1/78

Berger, E., Zauderer, A., Pooley, G. G., et al. 2012, ApJ, 748, 36, doi: 10.1088/0004-637X/748/1/36

Berton, M., Järvelä, E., Crepaldi, L., et al. 2020, A&A, 636, A64, doi: 10.1051/0004-6361/202037793

Blandford, R., Meier, D., & Readhead, A. 2019, ARA&A, 57, 467, doi: 10.1146/annurev-astro-081817-051948

Blandford, R. D., & Znajek, R. L. 1977, MNRAS, 179, 433, doi: 10.1093/mnras/179.3.433

Boller, T., Freyberg, M. J., Truemper, J., et al. 2016, VizieR Online Data Catalog, J/A+A/588/A103

Brown, J. S., Holoien, T. W. S., Auchettl, K., et al. 2017, MNRAS, 466, 4904, doi: 10.1093/mnras/stx033

Burrows, D. N., Hill, J. E., Nousek, J. A., et al. 2005, SSRv, 120, 165, doi: 10.1007/s11214-005-5097-2

Calzetti, D. 2013, in Secular Evolution of Galaxies, ed. J. Falcón-Barroso & J. H. Knapen, 419

Calzetti, D., Armus, L., Bohlin, R. C., et al. 2000, ApJ, 533, 682, doi: 10.1086/308692

Cenko, S. B., Krimm, H. A., Horesh, A., et al. 2012, ApJ, 753, 77, doi: 10.1088/0004-637X/753/1/77

Chabrier, G. 2003, PASP, 115, 763, doi: 10.1086/376392

Chambers, K. C., Magnier, E. A., Metcalfe, N., et al. 2016, arXiv e-prints, arXiv:1612.05560. https://arxiv.org/abs/1612.05560

Chevalier, R. A. 1998, ApJ, 499, 810, doi: 10.1086/305676

Cid Fernandes, R., Stasińska, G., Mateus, A., & Vale Asari, N. 2011, MNRAS, 413, 1687, doi: 10.1111/j.1365-2966.2011.18244.x

Clarke, T. E., Kassim, N. E., Brisken, W., et al. 2016, in Society of Photo-Optical Instrumentation Engineers (SPIE) Conference Series, Vol. 9906, Ground-based and Airborne Telescopes VI, ed. H. J. Hall, R. Gilmozzi, & H. K. Marshall, 99065B, doi: 10.1117/12.2233036

Cole, S., Percival, W. J., Peacock, J. A., et al. 2005, MNRAS, 362, 505, doi: 10.1111/j.1365-2966.2005.09318.x

Condon, J. J., Cotton, W. D., Greisen, E. W., et al. 1998, AJ, 115, 1693, doi: 10.1086/300337

Conroy, C., & Gunn, J. E. 2010, ApJ, 712, 833, doi: 10.1088/0004-637X/712/2/833

Conroy, C., Gunn, J. E., & White, M. 2009, ApJ, 699, 486, doi: 10.1088/0004-637X/699/1/486

Crumley, P., Lu, W., Santana, R., et al. 2016, MNRAS, 460, 396, doi: 10.1093/mnras/stw967

De, K., Kasliwal, M. M., Tzanidakis, A., et al. 2020, ApJ, 905, 58, doi: 10.3847/1538-4357/abb45c

Deller, A. T., Brisken, W. F., Phillips, C. J., et al. 2011, PASP, 123, 275, doi: 10.1086/658907

Domínguez, A., Siana, B., Henry, A. L., et al. 2013, ApJ, 763, 145, doi: 10.1088/0004-637X/763/2/145

Donley, J. L., Brandt, W. N., Eracleous, M., & Boller, T. 2002, AJ, 124, 1308, doi: 10.1086/342280

Drake, A. J., Djorgovski, S. G., Mahabal, A., et al. 2009, ApJ, 696, 870, doi: 10.1088/0004-637X/696/1/870

Eftekhari, T., Berger, E., Zauderer, B. A., Margutti, R., & Alexander, K. D. 2018, ApJ, 854, 86, doi: 10.3847/1538-4357/aaa8e0

Fabian, A. C. 2012, ARA&A, 50, 455, doi: 10.1146/annurev-astro-081811-125521

Falcke, H., Nagar, N. M., Wilson, A. S., Ho, L. C., & Ulvestad, J. S. 2001, in Black Holes in Binaries and Galactic Nuclei, ed. L. Kaper, E. P. J. V. D. Heuvel, & P. A. Woudt, 218, doi: 10.1007/10720995_45

Fender, R. 2010, in Lecture Notes in Physics, Berlin Springer Verlag, ed. T. Belloni, Vol. 794, 115, doi: 10.1007/978-3-540-76937-8_5

Fender, R., Koerding, E., Belloni, T., et al. 2007, arXiv e-prints, arXiv:0706.3838. https://arxiv.org/abs/0706.3838

Fender, R. P., Belloni, T. M., & Gallo, E. 2004, MNRAS, 355, 1105, doi: 10.1111/j.1365-2966.2004.08384.x

Fender, R. P., Gallo, E., & Russell, D. 2010, MNRAS, 406, 1425, doi: 10.1111/j.1365-2966.2010.16754.x

Fender, R. P., Homan, J., & Belloni, T. M. 2009, MNRAS, 396, 1370, doi: 10.1111/j.1365-2966.2009.14841.x

Foreman-Mackey, D., Hogg, D. W., Lang, D., & Goodman, J. 2013, PASP, 125, 306, doi: 10.1086/670067

Frank, J., & Rees, M. J. 1976, MNRAS, 176, 633, doi: 10.1093/mnras/176.3.633

Frederick, S., Gezari, S., Graham, M. J., et al. 2019, ApJ, 883, 31, doi: 10.3847/1538-4357/ab3a38

Granot, J., & Sari, R. 2002, ApJ, 568, 820, doi: 10.1086/338966

Greene, J. E., Strader, J., & Ho, L. C. 2020, ARA&A, 58, 257, doi: 10.1146/annurev-astro-032620-021835

Grupe, D., Komossa, S., Leighly, K. M., & Page, K. L. 2010, ApJS, 187, 64, doi: 10.1088/0067-0049/187/1/64

Gültekin, K., King, A. L., Cackett, E. M., et al. 2019, ApJ, 871, 80, doi: 10.3847/1538-4357/aaf6b9

Haardt, F., & Maraschi, L. 1991, ApJL, 380, L51, doi: 10.1086/186171

Hawkins, M. R. S. 2004, A&A, 424, 519, doi: 10.1051/0004-6361:20041127

HI4PI Collaboration, Ben Bekhti, N., Flöer, L., et al. 2016, A&A, 594, A116, doi: 10.1051/0004-6361/201629178

Ho, A. Y. Q., Phinney, E. S., Ravi, V., et al. 2019, ApJ, 871, 73, doi: 10.3847/1538-4357/aaf473

Intema, H. T., Jagannathan, P., Mooley, K. P., & Frail, D. A. 2017, A&A, 598, A78, doi: 10.1051/0004-6361/201628536

Janiuk, A., & Czerny, B. 2011, MNRAS, 414, 2186, doi: 10.1111/j.1365-2966.2011.18544.x

Jiang, N., Wang, T., Hu, X., et al. 2021, ApJ, 911, 31, doi: 10.3847/1538-4357/abe772

Johnson, B. D., Leja, J., Conroy, C., & Speagle, J. S. 2021, ApJS, 254, 22, doi: 10.3847/1538-4365/abef67

Kangas, T., & Fruchter, A. S. 2021, ApJ, 911, 14, doi: 10.3847/1538-4357/abe76b

Kewley, L. J., Groves, B., Kauffmann, G., & Heckman, T. 2006, MNRAS, 372, 961, doi: 10.1111/j.1365-2966.2006.10859.x

Koay, J. Y., Vestergaard, M., Bignall, H. E., Reynolds, C., & Peterson, B. M. 2016, MNRAS, 460, 304, doi: 10.1093/mnras/stw975

Komossa, S. 2018, in Revisiting Narrow-Line Seyfert 1 Galaxies and their Place in the Universe, 15. https://arxiv.org/abs/1807.03666

Komossa, S., Voges, W., Xu, D., et al. 2006, AJ, 132, 531, doi: 10.1086/505043

Krimm, H. A., Barthelmy, S. D., Markwardt, C. B., et al. 2006, in AAS/High Energy Astrophysics Division, Vol. 9, AAS/High Energy Astrophysics Division #9, 13.47

Kulkarni, S. R., Frail, D. A., Wieringa, M. H., et al. 1998, Nature, 395, 663, doi: 10.1038/27139

Kunert-Bajraszewska, M., Wołowska, A., Mooley, K., Kharb, P., & Hallinan, G. 2020, ApJ, 897, 128, doi: 10.3847/1538-4357/ab9598

Lacy, M., Baum, S. A., Chandler, C. J., et al. 2020, PASP, 132, 035001, doi: 10.1088/1538-3873/ab63eb

Laha, S., Reynolds, C. S., Reeves, J., et al. 2021, Nature Astronomy, 5, 13, doi: 10.1038/s41550-020-01255-2

Lähteenmäki, A., Järvelä, E., Ramakrishnan, V., et al. 2018, A&A, 614, L1, doi: 10.1051/0004-6361/201833378

Lang, D. 2014, AJ, 147, 108, doi: 10.1088/0004-6256/147/5/108

Levan, A. J., Tanvir, N. R., Brown, G. C., et al. 2016, ApJ, 819, 51, doi: 10.3847/0004-637X/819/1/51

Liska, M., Hesp, C., Tchekhovskoy, A., et al. 2021, MNRAS, 507, 983, doi: 10.1093/mnras/staa099

Lusso, E., Comastri, A., Simmons, B. D., et al. 2012, MNRAS, 425, 623, doi: 10.1111/j.1365-2966.2012.21513.x

Mainzer, A., Bauer, J., Grav, T., et al. 2011, ApJ, 731, 53, doi: 10.1088/0004-637X/731/1/53

Maity, B., & Chandra, P. 2021, ApJ, 907, 60, doi: 10.3847/1538-4357/abd2be

Matsuoka, M., Kawasaki, K., Ueno, S., et al. 2009, PASJ, 61, 999, doi: 10.1093/pasj/61.5.999

Mattila, S., Pérez-Torres, M., Efstathiou, A., et al. 2018, Science, 361, 482, doi: 10.1126/science.aao4669

McConnell, D., Hale, C. L., Lenc, E., et al. 2020, PASA, 37, e048, doi: 10.1017/pasa.2020.41

McMullin, J. P., Waters, B., Schiebel, D., Young, W., & Golap, K. 2007, in Astronomical Society of the Pacific Conference Series, Vol. 376, Astronomical Data Analysis Software and Systems XVI, ed. R. A. Shaw, F. Hill, & D. J. Bell, 127

Meisner, A. M., Lang, D., & Schlegel, D. J. 2017, AJ, 154, 161, doi: 10.3847/1538-3881/aa894e

Metzger, B. D., Williams, P. K. G., & Berger, E. 2015, ApJ, 806, 224, doi: 10.1088/0004-637X/806/2/224

Mineo, S., Gilfanov, M., Lehmer, B. D., Morrison, G. E., & Sunyaev, R. 2014, MNRAS, 437, 1698, doi: 10.1093/mnras/stt1999

Mooley, K. P., Hallinan, G., Bourke, S., et al. 2016, ApJ, 818, 105, doi: 10.3847/0004-637X/818/2/105

Narayan, R., & Yi, I. 1994, ApJL, 428, L13, doi: 10.1086/187381

Netzer, H., Mainieri, V., Rosati, P., & Trakhtenbrot, B. 2006, A&A, 453, 525, doi: 10.1051/0004-6361:20054203

Nyland, K., Dong, D. Z., Patil, P., et al. 2020, ApJ, 905, 74, doi: 10.3847/1538-4357/abc341

Oke, J. B., Cohen, J. G., Carr, M., et al. 1995, PASP, 107, 375, doi: 10.1086/133562

Osterbrock, D. E. 1991, Reports on Progress in Physics, 54, 579, doi: 10.1088/0034-4885/54/4/002

Panessa, F., & Bassani, L. 2002, A&A, 394, 435, doi: 10.1051/0004-6361:20021161

Pasham, D. R., Cenko, S. B., Levan, A. J., et al. 2015, ApJ, 805, 68, doi: 10.1088/0004-637X/805/1/68

Peters, W., Polisensky, E., Brisken, W., et al. 2021, in American Astronomical Society Meeting Abstracts, Vol. 53, American Astronomical Society Meeting Abstracts, 211.06

Planck Collaboration, Aghanim, N., Akrami, Y., et al. 2020, A&A, 641, A6, doi: 10.1051/0004-6361/201833910

Polisensky, E., Lane, W. M., Hyman, S. D., et al. 2016, ApJ, 832, 60, doi: 10.3847/0004-637X/832/1/60

Ravi, V., Dykaar, H., Codd, J., et al. 2021, arXiv e-prints, arXiv:2102.05795. https://arxiv.org/abs/2102.05795

Rees, M. J. 1988, Nature, 333, 523, doi: 10.1038/333523a0

Ricci, C., Trakhtenbrot, B., Koss, M. J., et al. 2017, Nature, 549, 488, doi: 10.1038/nature23906

Risaliti, G., Maiolino, R., & Salvati, M. 1999, ApJ, 522, 157, doi: 10.1086/307623

Rusinek, K., Sikora, M., Kozieł-Wierzbowska, D., & Godfrey, L. 2017, MNRAS, 466, 2294, doi: 10.1093/mnras/stw3330

Salas, P., Bauer, F. E., Stockdale, C., & Prieto, J. L. 2013, MNRAS, 428, 1207, doi: 10.1093/mnras/sts104

Sault, R. J., Teuben, P. J., & Wright, M. C. H. 1995, in Astronomical Society of the Pacific Conference Series, Vol. 77, Astronomical Data Analysis Software and Systems IV, ed. R. A. Shaw, H. E. Payne, & J. J. E. Hayes, 433. https://arxiv.org/abs/astro-ph/0612759

Soderberg, A. M., Chevalier, R. A., Kulkarni, S. R., & Frail, D. A. 2006, ApJ, 651, 1005, doi: 10.1086/507571

Soderberg, A. M., Chakraborti, S., Pignata, G., et al. 2010, Nature, 463, 513, doi: 10.1038/nature08714

Somalwar, J. J., Ravi, V., Dong, D., et al. 2021, arXiv e-prints, arXiv:2108.12431. https://arxiv.org/abs/2108.12431

Speagle, J. S. 2020, MNRAS, 493, 3132, doi: 10.1093/mnras/staa278

Tchekhovskoy, A., McKinney, J. C., & Narayan, R. 2009, ApJ, 699, 1789, doi: 10.1088/0004-637X/699/2/1789

Tchekhovskoy, A., Metzger, B. D., Giannios, D., & Kelley, L. Z. 2014, MNRAS, 437, 2744, doi: 10.1093/mnras/stt2085

Tchekhovskoy, A., Narayan, R., & McKinney, J. C. 2010, ApJ, 711, 50, doi: 10.1088/0004-637X/711/1/50

Tonry, J. L., Denneau, L., Heinze, A. N., et al. 2018, PASP, 130, 064505, doi: 10.1088/1538-3873/aabadf

van Velzen, S., Farrar, G. R., Gezari, S., et al. 2011, ApJ, 741, 73, doi: 10.1088/0004-637X/741/2/73

van Velzen, S., Gezari, S., Hammerstein, E., et al. 2021, ApJ, 908, 4, doi: 10.3847/1538-4357/abc258

Vattakunnel, S., Tozzi, P., Matteucci, F., et al. 2012, MNRAS, 420, 2190, doi: 10.1111/j.1365-2966.2011.20185.x

Voges, W. 1993, Advances in Space Research, 13, 391, doi: 10.1016/0273-1177(93)90147-4

Weiler, K. W., Panagia, N., Montes, M. J., & Sramek, R. A. 2002, ARA&A, 40, 387, doi: 10.1146/annurev.astro.40.060401.093744

Wiersema, K., Higgins, A. B., Levan, A. J., et al. 2020, MNRAS, 491, 1771, doi: 10.1093/mnras/stz3106

Wilson, W. E., Ferris, R. H., Axtens, P., et al. 2011, MNRAS, 416, 832, doi: 10.1111/j.1365-2966.2011.19054.x

Wołowska, A., Kunert-Bajraszewska, M., Mooley, K. P., et al. 2021, ApJ, 914, 22, doi: 10.3847/1538-4357/abe62d

Wright, E. L., Eisenhardt, P. R. M., Mainzer, A. K., et al. 2010, AJ, 140, 1868, doi: 10.1088/0004-6256/140/6/1868

Yang, J., Paragi, Z., van der Horst, A. J., et al. 2016, MNRAS, 462, L66, doi: 10.1093/mnrasl/slw107

York, D. G., Adelman, J., Anderson, John E., J., et al. 2000, AJ, 120, 1579, doi: 10.1086/301513

Zauderer, B. A., Berger, E., Margutti, R., et al. 2013, ApJ, 767, 152, doi: 10.1088/0004-637X/767/2/152

Zauderer, B. A., Berger, E., Soderberg, A. M., et al. 2011, Nature, 476, 425, doi: 10.1038/nature10366